Ore Geology Reviews 167 (2024) 105998

Contents lists available at ScienceDirect

Ore Geology Reviews

journal homepage: www.elsevier.com/locate/oregeorev

The application of PRISMA hyperspectral satellite imagery in the delineation of distinct hydrothermal alteration zones in the Chilean Andes: The Marimaca IOCG and the Río Blanco-Los Bronces Cu-Mo porphyry districts

Anna Sorrentino [a], Rita Chirico [b,*], Francesca Corrado [a], Carsten Laukamp [c], Diego Di Martire [a], Nicola Mondillo [a,d]

[a] Department of Earth, Environment and Resources Sciences, University of Naples Federico II, Naples, Italy
[b] Department of Geosciences, University of Padua, Padua, Italy
[c] CSIRO Mineral Resources, Kensington, WA, Australia
[d] Natural History Museum, London, UK

ARTICLE INFO

Keywords:
Hyperspectral analysis
PRISMA
Porphyry copper deposits
Iron oxide-copper–gold
Mineral mapping

ABSTRACT

This study provides an overview of the application of hyperspectral imagery acquired by the Italian satellite mission "PRecursore IperSpettrale della Missione Applicativa" (PRISMA), for mapping hydrothermal and supergene mineral alteration zones associated with different Cu deposits in the Chilean Andes. Study areas include the Marimaca Copper Project in the Naguayán district (Antofagasta Province), hosting Late Jurassic – Early Cretaceous iron oxide-copper–gold mineralizations and the Río Blanco-Los Bronces district (Santiago Region) known for its Late Miocene – Early Pliocene copper-molybdenum porphyry deposits. These mineral systems exhibit hydrothermal alteration haloes extending over several kilometers, with upward and outward mineral zonation.

To characterize the surface-exposed alteration, the satellite imagery was processed using a multiple feature extraction workflow targeting the relative abundances and compositions of specific supergene and hydrothermal alteration minerals, including Fe-oxides and hydroxides (hematite-goethite), phyllosilicates (micas-kaolinite-chlorite), hydroxyl-bearing sulfates (alunite-natroalunite-jarosite) and epidote. The results reveal a zonation from proximal sulfates (natroalunite to alunite) and Al-rich white mica (ranging from 0.3 km-wide for the area identified to the east of the Marimaca deposit to 1 km-wide in correspondence of the Los Sulfatos deposit, respectively) to distal Al-poor white mica (0.2 to 0.5 km-wide, respectively) and an outer chlorite-epidote zone. In the Marimaca Project area, the structurally-controlled alteration evolves west to east from chlorite-rich to phengitic white mica (Al-poor). A NNE-SSW trending supergene leached cap covers a 6 km-long and up to 2 km-wide area from north to south. Our study documents how spaceborne hyperspectral imaging spectroscopy can support mineral exploration by enabling non-invasive reconnaissance mapping of the outcropping rocks, providing specific targeting information for follow-up field surveys and drilling campaigns.

1. Introduction

During the past decade, the hyperspectral remote sensing technology has been established as a robust tool for the interpretation of outcropping mineral assemblages and lithological units, with important implications for the mineral exploration and ore deposits characterization (Taranik and Aslett, 2009; Bedini, 2017; Peyghambari and Zhang, 2021). The present study interprets data from the Italian Space Agency's (ASI) PRISMA mission, which is part of a new generation of VNIR-SWIR hyperspectral satellite sensors that have not yet undergone a comprehensive evaluation for geological mapping and mineral exploration. In particular, the PRISMA data are here used for mapping distinct alteration haloes associated with porphyry Cu and Iron Oxide-Copper-Gold (IOCG) deposits in the Chilean Andes. The hydrothermal wall-rock

* Corresponding author.
E-mail address: rita.chirico@unipd.it (R. Chirico).

https://doi.org/10.1016/j.oregeorev.2024.105998
Received 5 February 2024; Received in revised form 19 March 2024; Accepted 20 March 2024
Available online 21 March 2024

alteration zones characterizing these deposit types (e.g., Sillitoe, 2010), that are commonly used for vectoring toward the cores of the mineralized systems, are highly suitable targets for satellite-based remote sensing surveys, due to their diagnostic mineral compositions and often large (kms wide) alteration haloes.

Porphyry Cu(-Mo) and IOCG deposits represent the two most significant sources of copper in the Chilean Andes, followed by stratabound Cu(-Ag) ores, also known as manto-type Cu(-Ag) mineralization, and massive magnetite deposits (Zentilli, 2022). These deposits are genetically associated with subduction-related Andean arc magmatism (Sillitoe, 2003; Sillitoe and Perelló, 2005; Maureira et al., 2022). Porphyry Cu (-Mo) deposits are S-rich ores consisting of veins and disseminations of chalcopyrite, bornite ± molybdenite and pyrite (e.g., Sillitoe, 1972, 2010; Richards, 2009). IOCG deposits have been first described by Hitzman et al. (1992) and have become research objectives over the past few years. IOCGs differ in some important characteristics from porphyry Cu(-Mo), being mainly Fe-oxide rich (magnetite and/or hematite > 10 %) deposits, with chalcopyrite and minor bornite (±Au, Ag) as economic minerals. Their origin is mostly considered to be related to the migration of "oxidized", acid and sulfide-poor hydrothermal metal-bearing fluids through structural lineaments (faults and/or shear zones) and to the precipitation of metals into "reduced" traps (Williams et al., 2005; Groves et al., 2010; Chen, 2013; Richards and Mumin, 2013; Kreiner and Barton, 2017).

The application of multispectral and hyperspectral remote sensing technologies to the exploration of porphyry Cu-Mo deposits is long-established, and in the past, it was the focus of many studies, most of them intended for mapping the hydrothermal host-rock broad alteration patterns characteristic of this deposit-type (Bedini, 2017; Peyghambari and Zhang, 2021, and references therein; Portela et al., 2021). Several studies have been conducted using multispectral data from the space-borne missions Landsat, Sentinel-2, WorldView-3 (WV-3) to map the alteration mineral distribution yielding satisfactory results (Abrams et al., 1983; Pour and Hashim, 2012; Chen et al., 2021; Ishagh et al., 2021). Notably, the free-of-charge Japanese Advanced Spaceborne Thermal Emission and Reflection Radiometer (ASTER) mission aboard the US TERRA platform (https://terra.nasa.gov/), which features a 14-band spectral resolution spanning from Visible Near (VNIR) – Short wave (SWIR) to the Thermal Infrared (TIR) regions, facilitated a comprehensive analysis of alteration minerals and their distribution (e.g., Cudahy et al., 2008, Pour and Hashim, 2012; Cudahy, 2016; Chen et al., 2021; Ishagh et al., 2021). However, multi-spectral systems with SWIR-2 spectral resolutions > 40 nm, such as ASTER, are insufficient for remote detection of < 20 nm wavelength changes, rendering hyperspectral data a more suitable alternative (Cudahy, 2016). For example, by using the AVIRIS airborne hyperspectral data, Berger et al. (2003) detected sericitic, argillic and propylitic mineral alteration zones associated with the Red Mountain and Sunnyside deposits in Arizona. By using Hyperion EO-1 spaceborne data, Zadeh et al. (2014) could map the alteration systems associated with porphyry deposits, despite the moderate spatial resolution (30 m/pixel) and low signal-to-noise ratio of the sensor. Kokaly et al., (2017a) and Graham et al. (2018) through a multiscale approach from field-based and laboratory-level spectroscopy to airborne hyperspectral imaging (HyMap; HyVista Corporation), performed characterization and mapping of the alteration zones occurring at the Orange Hill and Bond Creek Porphyry Cu-Mo deposits (Alaska). These authors focused on the identification of spectrally dominant minerals, like white micas, chlorite, clays and sulfates, paying special attention to the 2200 nm absorption feature and its wavelength position. In this latest specific case study, the shifting to longer wavelengths observed at airborne viewing scale gave the authors critical information, resulting in the discrimination between the white mica associated with the porphyry deposit formation (long wavelength, Al-poor or "phengitic") compared to the Al-rich white mica associated with plutonic and volcanic arc rocks not affected by magmatic-hydrothermal fluids.

Similarly to the previous cases, the hydrothermal alteration patterns and the iron oxide zonation associated with IOCG deposits have also been investigated through remote sensing in recent times (Corriveau, 2007; Mount Isa Inlier, Laukamp et al., 2011). Several applications of reflectance spectroscopy to the study of IOCG deposits mainly focused on the characterization of the 2200 nm absorption feature, to discriminate potassic alteration patterns, as well as defining variable intensity degrees of sericitic alteration associated with ore forming processes (e.g., variation of aluminum content of phengite in Olympic Dam IOCG deposit, Tappert et al., 2013), and on the identification of opaque phases for detecting "reduced" rock types (e.g., Starra area, Mount Isa Inlier, Cudahy, 2016).

Literature regarding lithological mapping and geological application using the recently launched (2019) PRISMA hyperspectral satellite is quickly growing up, intending to evaluate and validate PRISMA for various geological purposes, for example: (1) remote identification of CO_2 emissions (Romaniello et al., 2021, 2022) and (2) methane emission points (Guanter et al., 2021); (3) identification and mapping regolith and supergene and hydrothermal alteration minerals (e.g., the Cuprite deposit in Nevada, Bedini and Chen, 2020; the Jabali deposit area in Yemen, Chirico et al., 2022; the Rocklea Dome area in Western Australia, Laukamp, 2022; the Ondoto carbonatite complex in Namibia, Kopackova-Strnadova et al., 2023), and (4) lithological mapping (e.g., the Makhtesh Ramon national park area in Israel, Heller Pearlshtien et al., 2021; Laukamp, 2022). Nonetheless, the PRISMA data remains unexplored with respect to the mineralogical characterization of porphyry-Cu deposits and IOCG mineralization.

During the past decade, the availability of VNIR-SWIR imaging spectroscopy data from space has significantly increased. Several orbital hyperspectral remote sensing missions involving various space agencies are in operational phase, for instance the ASI's PRISMA, the German Aerospace Center's (DLR) DLR Earth Sensing Imaging Spectrometer (DESIS) and Environmental Mapping and Analysis Program (EnMAP), as well as the Hyperspectral Imager Suite (HISUI) of the Japanese Ministry of Economy, Trade, and Industry (METI) and the NASA's Earth Surface Mineral Dust Source Investigation (EMIT) missions, while others are in advanced stages of development.

The new generation of hyperspectral imaging sensors, including PRISMA, are notable for their high spectral resolution, which includes hundreds of spectral bands covering the VNIR-SWIR range. The DLR's EnMAP system is characterized by 235 bands in the 420–2450 nm range and 30 m GSD, while NASA's EMIT has 280 bands ranging from 380 to 2500 nm with a 60 m GSD, and the Japanese HISUI offers up to 20 m/pixel VNIR-SWIR products with a mean spectral resolution around 11 nm. In contrast to the first hyperspectral VNIR-SWIR satellite sensor, Hyperion, the signal-to-noise ratio of the new generation of hyperspectral satellite sensors is much higher, vastly improving the ability to characterize mineral species and mineral composition. The abundance of spectral information provided by these new sensors enables the collection of continuous data across the entire spectral range, in contrast to multispectral sensors, which sample discrete wavelength intervals. This capability allows for improved discrimination of surface features compared to the multispectral sensors mentioned earlier. For example, PRISMA is valuable for the identification and geochemical characterization of several minerals which are common products of both supergene and hydrothermal alteration associated with porphyry-Cu(-Mo) and IOCG ore-type systems (Sillitoe, 2010), because these phases exhibit diagnostic absorption features in the VNIR-SWIR wavelength region covered by the satellite system. These minerals are: Fe-oxides and hydroxides, micas (muscovite and phengite), clays such as kaolinite and pyrophyllite, chlorite-epidote, and sulfates like alunite and jarosite (e.g., Spatz, 1996; Tangestani and Moore, 2002; Berger et al., 2003; Bishop and Murad, 2005; Mars and Rowan, 2006; Riley et al., 2007; Pour and Hashim, 2012; Bedini, 2017; Laukamp et al., 2021; Thiele et al., 2021, among others).

The present study aims at: 1) evaluating the capability of PRISMA satellite hyperspectral imagery for mineral exploration, by inspecting its

performances in alteration mineral mapping, since it can represent a rapid and cost-effective mean for gaining and revealing similar information from regional to district scale; 2) identifying the alteration assemblages for vectoring to the mineralized bodies, possibly defining new exploration targets in the considered areas suitable for follow-up investigations. Two test areas were chosen: (1) the Marimaca Copper Project area (Costal Cordillera, Antofagasta Region, northern Chile), and (2) the Río Blanco-Los Bronces copper-molybdenum porphyry district (Central Andes, Santiago Region) (Toro et al., 2012; Piquer et al., 2015). The areas were selected as test sites mainly because of the almost total absence of vegetation cover and, above all, the well-known, well-exposed and extended hydrothermal upward and outward zonation patterns displayed by the host rocks in the surroundings of orebodies. The Río Blanco-Los Bronces Cu-Mo Porphyry district was considered as a "validation site" for the present study, since the detailed mineralogical mapping of the hydrothermal alteration patterns has been published (Irarrazaval et al., 2010; Toro et al., 2012), and allowed to test the accuracy of the satellite mineral maps - this makes not strictly necessary to have validation ground samples. For the Marimaca deposit area, on the other hand, published alteration mineral distribution maps are quite limited, therefore a few descriptions of the geological features and the mineralization characteristic, distribution and composition occurring in the exploration reports (Kalanchey et al., 2020) were used to cross-check the satellite maps.

The methodology that we used is based on the combination of single feature extraction indices (or band ratios) into multiple feature extraction workflow applied to the PRISMA hyperspectral scenes with the specific objective of: 1) mapping large footprint alteration signatures (km scale), by extracting white micas, chlorite (and epidote), kaolin group minerals and sulfates (alunite and jarosite) and Fe-oxides and hydroxides relative abundances, and 2) identifying compositional variation for white micas, and evaluating compositional variations for alunite.

2. Regional geology

The Central Andes of Chile are characterized by four longitudinal metallogenic belts that are the host for a broad spectrum of economically Cu deposits and prospects, containing also great quantities of other elements such as Fe, Au, Pb-Zn, Ag, or Mn (Sillitoe, 2003; Sillitoe and Perelló, 2005). Each belt developed progressively from west to east, during distinct metallogenic periods, as a result of the eastward migration of arc magmatism (Sillitoe et al., 1982; Beckinsale et al., 1985; Clark et al., 1990a; Noble and McKee, 1999; Gendall et al., 2000; Sillitoe and Perelló, 2005; García et al., 2017; Cabello, 2021). The epochs span from Middle - Late Mesozoic on the Pacific coast to Miocene - Early Pliocene along the eastern border of the orogen, at the Chile - Argentina boundary (Figs. 1a and 2a) (Sillitoe, 2003; Sillitoe and Perelló, 2005; Cabello,

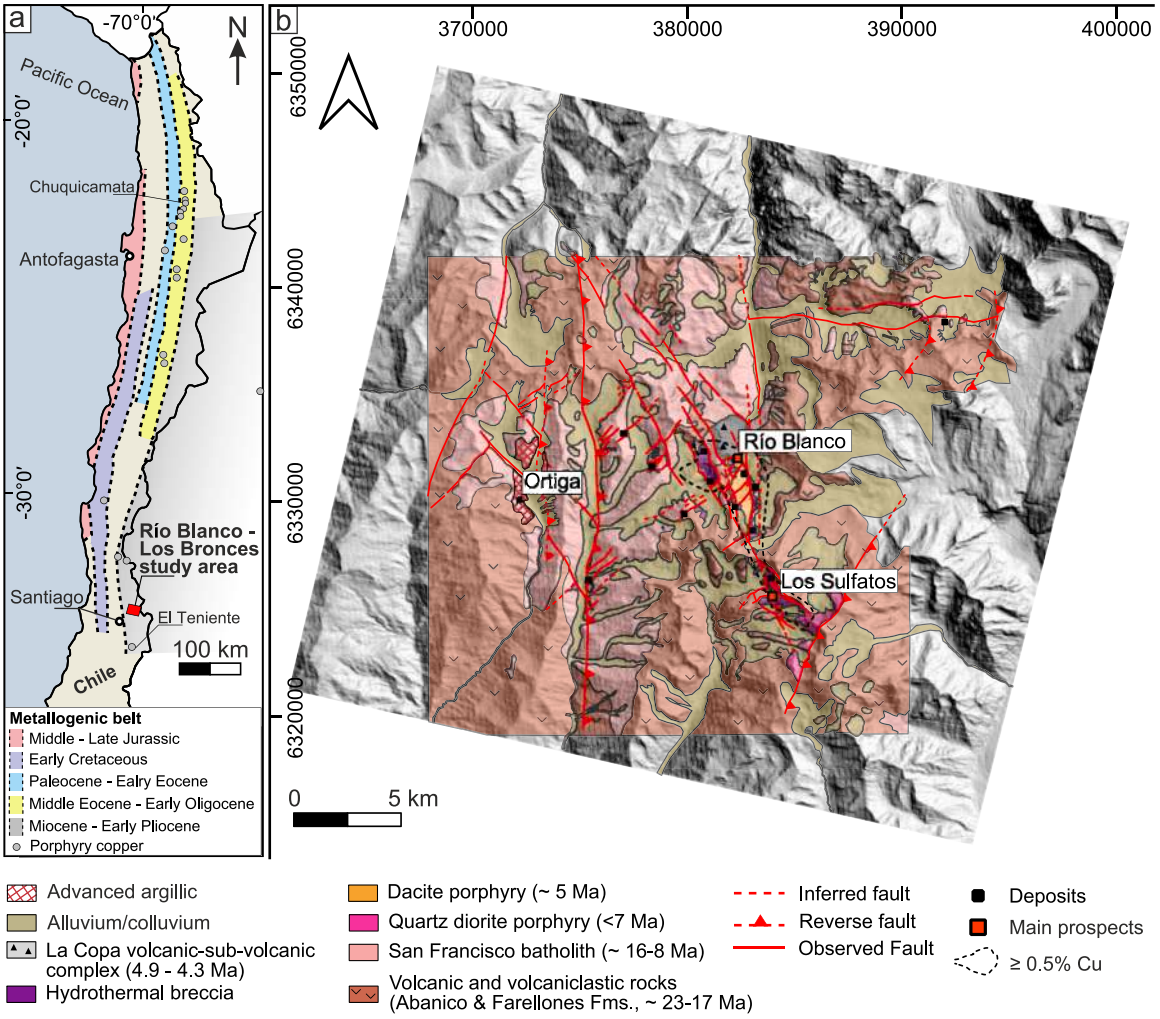

Fig. 1. (a) Location of PRISMA image covering the Río Blanco-Los Bronces study area, main porphyry copper deposits, metallogenic belts and epochs are indicated (modified from Sillitoe, 1988; Sillitoe and Perelló 2005); (b) Simplified geological map of the Río Blanco-Los Bronces Porphyry Cu-Mo district (modified from Toro et al., 2012) showing only the area corresponding to the one covered by PRISMA. Coordinate Reference System: WGS 84 / UTM zone 19S.

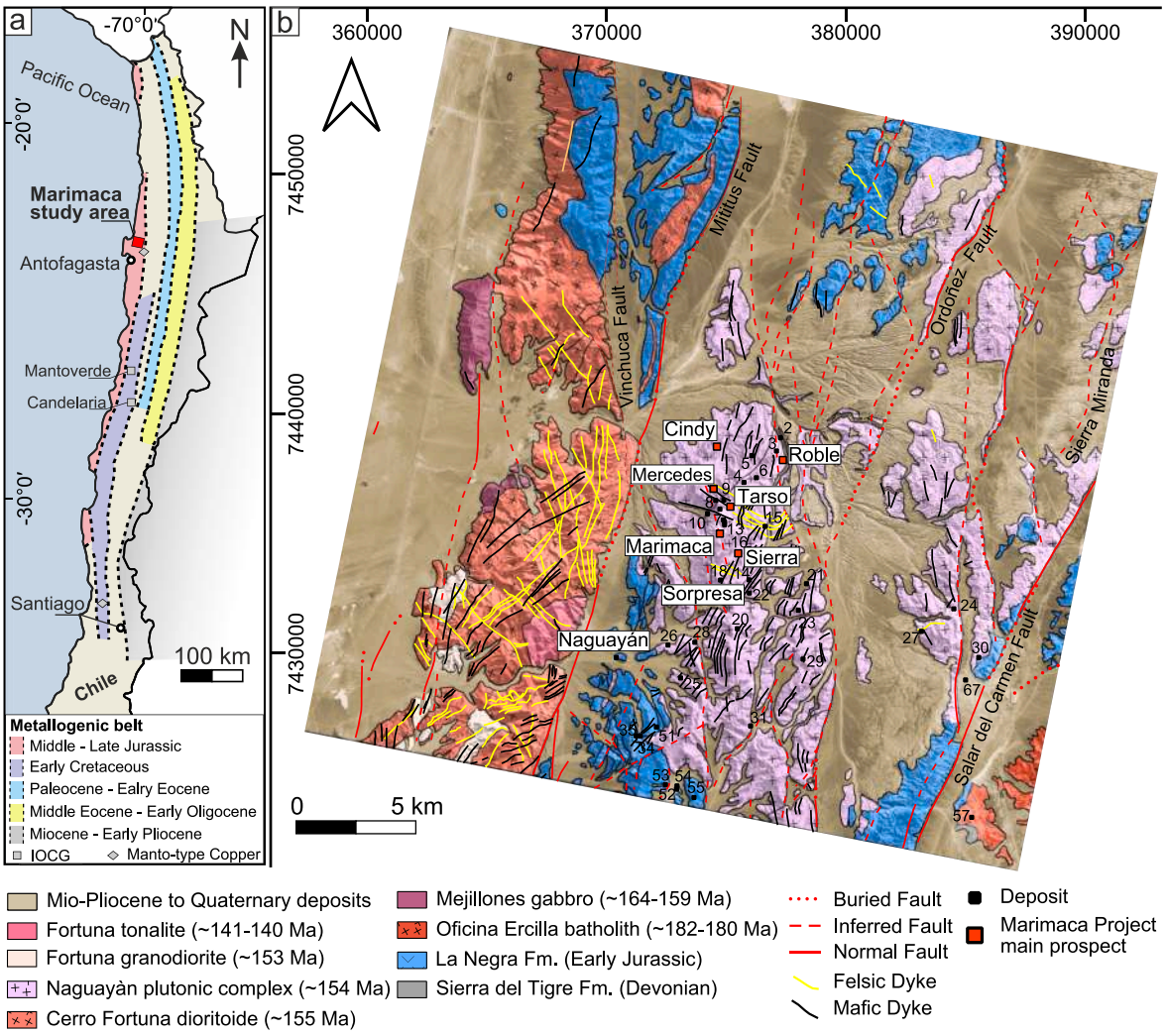

Fig. 2. (a) Location of PRISMA image covering the Marimaca Copper Project area, IOCG, manto-type deposits, metallogenic belts and epochs are indicated (modified from Sillitoe, 1988; Sillitoe and Perelló 2005); (b) Simplified geological map of the Marimaca study area (modified from Cortés et al., 2007) showing only the area corresponding to the one covered by PRISMA. Coordinate Reference System: WGS 84 / UTM zone 19S.

2021).

The Mesozoic belt extends semi-continuously along the Coastal Cordillera of northern Chile with an average thickness of about 30 km and hosts one of the world's major IOCG belts (including deposits like Marimaca, Candelaria-Punta del Cobre and Mantoverde; Marschik and Fontboté, 2001; Benavides et al., 2007) (Fig. 2a), these deposits are spatially associated with minor Cu-poor massive magnetite mineralization, manto-type Cu (e.g., Mantos Blancos and El Soldado; Wilson et al., 2003; Ramírez et al., 2006) and subordinate porphyry-Cu deposits (e.g., Andacollo; Llaumett et al., 1975; Munizaga et al., 1985). The formation of IOCG deposits took place under extensional and transtensional tectonic regimes, developed in response of retreating convergent margin (slab roll-back) and high-angle subduction of the Phoenix plate. During the Early Cretaceous, maximum crustal thinning occurred, causing a peak in the development of IOCGs accompanied by greater metal enrichments (Sillitoe, 2003; Chen, 2013). From the Late Cretaceous, compressive tectonic pulses inverted most of the structures (fault and back-arc basin), probably triggered by the final opening phases of the Atlantic Ocean and the decrease of the subduction angle at the Chilean trench (Mpodozis and Ramos, 1989; Larson, 1991; Ladino et al., 1997), causing intense shortening and thickening of the upper crust. This resulted in a drastic reduction in the formation of IOCG, massive magnetite and manto-type deposits, and creating favorable conditions for the genesis and development of porphyry-Cu systems. The formation of the Chilean porphyry Cu (-Mo, -Au) deposits (e.g., Cerro Colorado, Spence, Chuquicamata, Esperanza, Escondida; Río Blanco–Los Bronces, El Teniente; Ossandón et al., 2001; Rowland and Clark, 2001; Bouzari and Clark, 2002; Cotton III, 2003; Maksaev et al., 2004; Deckart et al., 2005; Padilla-Garza et al., 2005; Sillitoe and Perelló, 2005), along with small Cu (±Mo-Au-Ag) veins and tourmaline breccia-pipes, occurred from the Paleocene to Early Pliocene during relatively short time spans (lasting about 10 – 20 m.y.; Fig. 1a).

2.1. *The Río Blanco-Los Bronces district*

The giant Río Blanco-Los Bronces Porphyry Copper-Molybdenum district is located approximately 50 km northeast of Santiago. The district falls within the easternmost metallogenic belt of Late Miocene to Early Pliocene age and covers an area of ~ 15 km^2 (Fig. 1a) (Toro et al., 2012). The Río Blanco deposit is an underground mine owned by the Andina Division of the state-owned Codelco-Chile, whereas the Los Bronces deposit is an open pit mine held by the Anglo American Sur. In 2009, the overall production amounted to 448150 t Cu and 2163 t Mo (Deckart et al., 2014).

The porphyries are hosted by volcanic and volcanoclastic rocks of the Abanico and Farallones Formations (~23 – 17 Ma; Fig. 1b), deposited, respectively, during the phases of opening and subsequent inversion of the Abanico Basin (Piquer et al., 2015). These formations were intruded

by numerous plutonic rocks of Miocene to Pliocene age, like the large San Francisco batholith (~16 – 8 Ma; Fig. 1b), a granodiorite-dominated complex extending at surface over an area of at least 200 km^2 (Warnaars et al., 1985; Toro et al., 2012). The major Cu(-Mo) mineralization was associated with the emplacement of several porphyry intrusions centered on the east side of this batholith, whose position was controlled by closely spaced N-NW-trending basement faults defining structural corridors (Warnaars et al., 1985; Toro et al., 2012). The copper-iron-molybdenum sulfides occur as quartz-vein stockworks and disseminations as well as vertically continuous hydrothermal tourmaline breccia complex (Warnaars et al., 1985; Serrano et al., 1998; Ricardo et al., 1999; Skewes et al., 2002; Deckart et al., 2005; Irarrazaval et al., 2010). The mineral system exhibits, at district-scale, a typical vertical and lateral hydrothermal zonation pattern with remnants of high sulfidation and/or advanced argillic assemblages at shallow levels, surrounded by sericite-illite, whereas K-silicate alteration assemblages are mainly present in association with chalcopyrite-bornite and chalcopyrite-pyrite at depth (Sillitoe and Perelló, 2005). Following breccia formation, magmatic activity was characterized by late mineral dacite porphyry intrusions culminated in the post-mineral intrusive and extrusive La Copa rhyolite breccia complex (Fig. 1b) (Irarrazaval et al., 2010).

The Los Bronces – Río Blanco area was affected by at least three porphyry-related hydrothermal alteration-mineralization and associated hydrothermal-breccia events (Irarrazaval et al., 2010). The breccia cement displays a vertical hydrothermal zonation, varying from quartz, sericite, tourmaline with pyrite > chalcopyrite, in the upper levels, to biotite, K-feldspar with chalcopyrite, bornite > pyrite, in the deeper levels (Toro et al., 2012).

The Los Sulfatos area is centered on an extensive igneous to magmatic-hydrothermal breccia complex, related to the La Paloma and Los Sulfatos main porphyry centers (Irarrazaval et al., 2010; Toro et al., 2012). The hydrothermal breccia complex is cemented by tourmaline near surface and by biotite at depth. At shallow levels, the cement breccia is distinctly affected by sericitic alteration and contains chalcopyrite – pyrite, minor tennantite-tetrahedrite, galena, sphalerite and ankerite that make up high-grade copper bodies (on average ~ 3—15 % Cu). The porphyry centers at Los Sulfatos and La Palomas are also characterized by peripheral chlorite alteration partially overprinting the potassic alteration in the core of the system. Remnants of advanced argillic haloes (kaolinite, alunite) are also preserved (Irarrazaval et al., 2010).

The Río Blanco-Los Bronces district is characterized by secondary enrichment and leached capping with presence of Fe-oxides and hydroxides, limited to a restricted area, whose shape and depth suggest that the supergene processes are related to the present vadose-water downflow due to snowmelt during summer months and are still active (Warnaars et al., 1985; Sillitoe, 2005).

2.2. The Marimaca Copper Project

The Marimaca Copper Project is located in the Antofagasta Province, approximately 45 km north of Antofagasta and 1250 km north of Santiago, within the Mesozoic Coastal Cordillera in the Naguayán district (Fig. 2a). The geographic UTM coordinates of the center of the area are 374,820 E and 7,435,132 S (Zone 19S, Datum WGS84) and the zone is characterized by minimal vegetation cover. The project is held 100 % by the Marimaca Copper Corporation, the concession covers an area of 742 km^2, subdivided in two packages: the Marimaca area (625 km^2) and the Iván area (116 km^2).

The Marimaca mine was active from the 1990 s to the mid-2000 s, through underground mining and small-scale artisanal pits that have produced around 100 Mt of copper oxides between 1 and 2 % of Cu. In 2022, the estimated mineral resources (measured plus indicated) were 140 Mt at 0.48 % Cu (Oviedo, 2022). Since 2016, the mining company has been reassessing historical drilling and conducting new drilling, geological mapping, sampling and geophysical surveying to define the geological model and the sulfide potential under the Marimaca deposit and in the surrounding areas. The results of the aeromagnetic survey, conducted over an area of 2 x 2 km, show a large magnetic anomaly extending at least 700 m depth below the mineralized area and that is controlled by west–northwest-trending fault systems (Kalanchey et al., 2020).

The local geology consists mainly of Jurassic volcanic and intrusive rocks, overlaying sporadic outcropping of the oldest Devonian metasedimentary formation (Sierra del Tigre) (Fig. 2b) (Cortés et al., 2007). The first evidence of the establishment of a subduction-related magmatic belt is the emplacement of thick basaltic to andesitic volcanic sequence of the La Negra Formation (Sinemuriano – Titoniano; Fig. 2b), which evolved over the time from tholeiitic to calc-alkaline affinity (Kramer et al., 2005; Cortés et al., 2007). The Lower Jurassic – Early Cretaceous plutonic rocks, also of calc-alkaline affinity, comprise diorite, monzonite and monzodiorite, with lesser gabbro, quartz monzonite and metadiorite bodies (Fig. 2b) (Cortés et al., 2007). The intrusions belonging to the Naguayán Plutonic Complex (~154 Ma) and the associated dyke swarms of gabbro through rhyodacite composition, characterized by variable orientation ranging from oldest to youngest, from northeast–southwest to north– south, to northwest–southeast, display close relationship with the Fe Oxide-Cu-Au mineralizing systems in the area (Fig. 2b) (Cortés et al., 2007; Kalanchey et al., 2020). Alluvial and marine deposits of Mio-Pliocene to Quaternary age overlie all the mentioned units (Fig. 2b) (Cortés et al., 2007). The main tectonic structure is represented by the Atacama Fault Zone (AFZ), which is an arc-parallel wrench fault system extending for > 1000 km along the Coastal Cordillera (Scheuber and Andriessen, 1990). To the west, the Naguayán Banded Fracture Belt (NBFZ) forms a wide zone of subparallel faults and fractures (around 15 km-long and 3 km-wide) with trend north–south to north–northeast, dipping at 40–60° to the east or southeast, to which is associated the emplacement of pre-mineral mafic dykes and, subsequently, that of the mineralization (Kalanchey et al., 2020).

The Marimaca deposit has affinities mainly with vein-style IOCG deposits and subordinately with “manto-type” mineralization styles. The mineralization is structurally controlled by fractures of the NBFZ and displays a hydrothermal ore style, occurring as massive orebodies, veins, stockworks and breccias. The mineral assemblage consists mainly of chalcopyrite, as the major copper-bearing mineral, moderate to minor pyrite, minor bornite, covellite and primary chalcocite (Kalanchey et al., 2020; Oviedo, 2022). The emplacement of hypogene orebodies is preceded and accompanied by hydrothermal alteration, characterized by regional calcic–sodic metasomatism with albite replacing plagioclase and actinolite and magnetite replacing mafic minerals. Further alteration minerals range from chlorite and epidote to sericite and hematite in the proximal zone to precious metals, following the common alteration pattern proposed by Hitzman et al. (1992) and subsequently modified by Sillitoe (2003), Williams et al. (2005) and specifically by Kreiner and Barton (2017) for sulfur-poor IOGC systems. Towards the east of the eastern limit of the main mineralized area, the so-called “hanging wall alteration front” controls the mineralization toward the top of the parallel-fractured monzonite and diorite units and dykes-related orebodies and marks the beginning of a prominent alteration characterized by more hematite than magnetite, a well-developed argillic halo and intense albitization. The feeder zones close to the hanging wall alteration display white clay (albite–sericite) and minor chlorite-hematite haloes (Oviedo, 2017; Kalanchey et al., 2020; Oviedo, 2022). Towards west of the mineralization, the “footwall alteration” consists of more actinolite and magnetite, chlorite haloes and variable degrees of albitization (Oviedo, 2017, 2022).

The Marimaca area has undergone supergene oxidation resulting in the formation of an enriched zone of secondary sulfides, overlaying the primary mineralization, and of a limonitic leached cap which comprises Fe oxy-hydroxides (hematite and goethite), deriving from the alteration of pyrite and magnetite, with minor clays and gypsum, and occurrences

of jarosite as haloes surrounding the northwest-trending faults. The oxide zone is exposed on surface and extends around 150 – 300 m in depth (Kalanchey et al., 2020).

3. Data and methods

3.1. The PRISMA hyperspectral data: Characteristics and processing

The hyperspectral PRISMA scenes covering the Marimaca and Río Blanco-Los Bronces-Los Sulfatos districts were acquired and downloaded from the PRISMA mission website (PRISMA data portal - https://www.prisma.asi.it; accessed on 2 February 2022) at respectively (1) 14:58:05 on 26 January 2022 (UTC), and (2) at 14:43:24 a.m. on 17 February 2022 (refer to Table A1 for the acquisition conditions of the analyzed scenes). The Level 2C products, already corrected for the atmospheric effects (Bottom-Of-Atmosphere reflectance; see product specifications for more details at www.prisma.asi.it) (ASI, 2020), were analyzed by several pre-processing and processing steps carried out using ENVI 5.6.2 software with the aim of obtaining hyperspectral mineral maps (Fig. 3). The VNIR and SWIR bands were first adjusted to improve geolocation accuracy, then corrections and filters were applied for orthorectification, cross-track illumination and smoothing. Subsequently, pixels that most likely do not contain the target minerals (e.g., areas characterized by alluvial-colluvial cover), and areas affected by shadows or belonging to non-geological materials (mainly vegetation, snow and man-made features), were masked and excluded (Fig. 3). More comprehensive details of the employed methodology can be found in the Appendix.

3.2. The multiple feature extraction method applied to the PRISMA hyperspectral images

The VNIR-active minerals absorptions are mainly caused by electronic processes, like the Charge Transfer Feature (CTF) and the Crystal Field Absorption Feature (CFA) in, for example, iron oxides (Curtiss, 1985; Morris et al., 1985; Burns, 1993; Cudahy and Ramanaidou, 1997). Three other processes, instead, cause the absorption features in the SWIR region (e.g., Laukamp et al., 2021): (1) first overtones of fundamental stretching vibrations of hydroxyl groups ($2\nu OH$) in hydroxyl-bearing minerals or a combination band of the OH-related stretching fundamental and a first overtone of a H_2O-related bending vibration ($2\delta H_2O$); (2) combinations ($\nu + \delta OH$) of hydroxyl-related fundamental stretching (νOH) and bending vibrations (δOH), and (3) CO_3-related combinations (e.g., $2\nu_3 + \nu_1$ CO_3) or overtones (e.g., $3\nu_3 CO_3$) of fundamental stretching vibrations.

Looking at the specific minerals of interest, white micas (e.g., muscovite, phengite, paragonite) and Al-bearing smectites (e.g., montmorillonite, beidellite) comprise a wide and variable group of minerals characterized by the main absorption feature at ~ 2200 nm (Al-OH) (Laukamp et al., 2021; Meyer et al., 2022). The position of this feature is assumed to be proportional to the octahedral cation composition of white mica and Al-smectites, following the coupled octahedral–tetrahedral Tschermak exchange (Mg, Fe^{2+})^{VI} + Si^{IV} ↔ Al^{IV} + (Al, Fe^{3+})^{VI} (Velde, 1965; Duke, 1994; Laukamp et al., 2021; Meyer et al., 2022). The exchange of divalent and trivalent Fe, Mg and/or Al in the octahedral layer (M−site) results in variations of the M−OH bond length, causing a shift of the 2200 nm absorption feature towards shorter (Al-rich) or longer (Al-poor) wavelengths. The investigation of this shift can give useful information regarding the type and intensity of the alteration, as well as for defining pH/geochemical gradients of the metallogenetic fluids (Halley et al., 2015; Wang et al., 2017; Meyer et al., 2022). Similarly, variations in the position of the feature at around 2160 nm, at either ~ 2159 or ~ 2170 nm, allow for the characterization of kaolinite and alunite, respectively, associated with the evaluation of the presence and shifting of features at ~ 1480 (OH bonds) and ~ 1760 nm (SO_4^{2-} bonds) characteristic of sulfates (like alunite). The shift in this secondary absorption feature at 1480 nm is due to the contrasting bond length/strength of K^+ and Na^+ linked to OH groups. Specifically, an absorption feature around 1470 nm suggests the presence of alunite, while an absorption nearing 1495 nm suggests the presence of

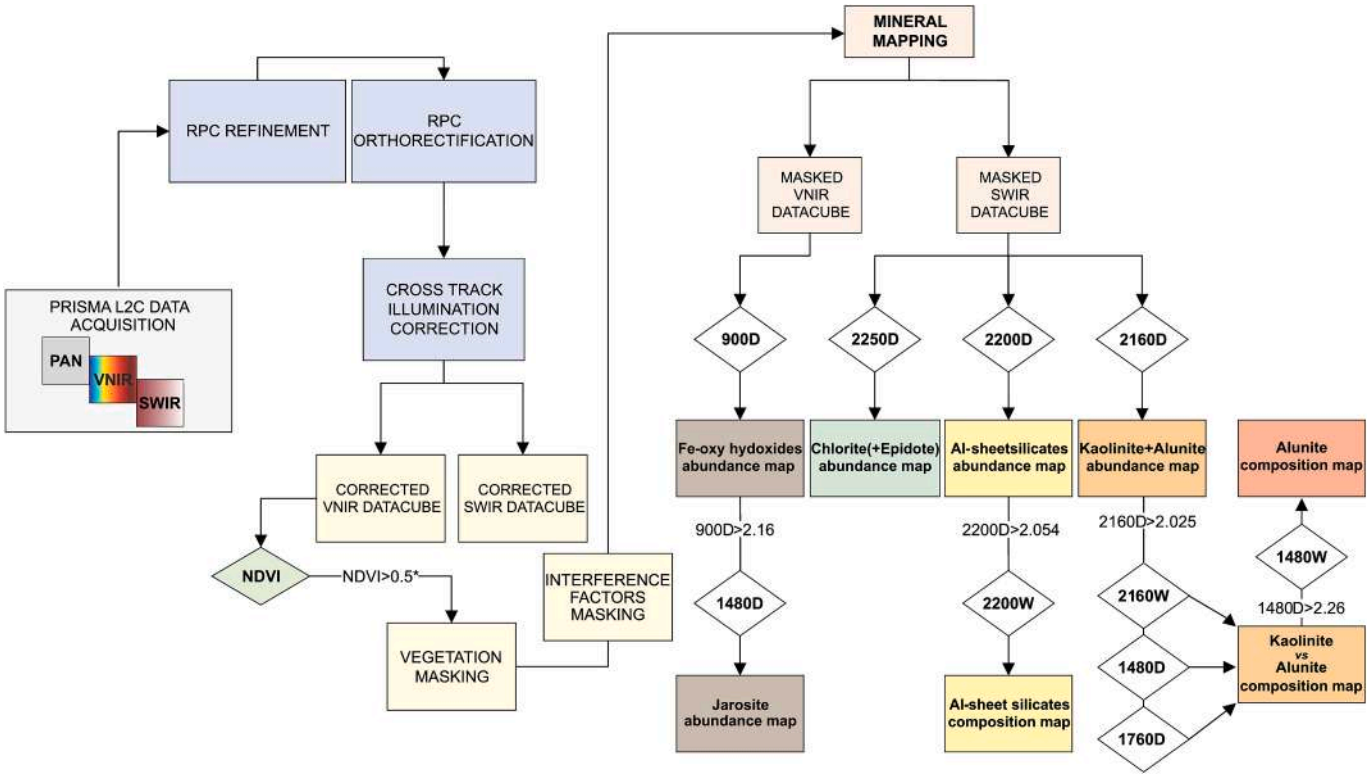

Fig. 3. Schematic workflow showing the pre-processing steps and the multiple feature extraction method used in this study.

natroalunite (Clark et al., 1990b; Thompson et al., 1999; Kerr et al., 2011; Arbiol and Layne, 2021). This characteristic provides information about the temperature of formation and can help in vectoring toward the center of the mineral system (Laukamp et al., 2021; Bishop and Murad, 2005; Stoffregen and Cygan, 1990).

These characteristics of absorption features can be determined and characterized from reflectance spectra through the application of spectral indices and band ratios. The hyperspectral products obtained using the band ratio method allow the visualization of wavelength position variation (chemical composition) and absorption depth (absolute intensity) of diagnostic features shown along the spectral signatures of rock-forming and alteration minerals defining each pixel of the hypercube acquired in the study area. The minerals features considered for this study for mineral mapping are referenced in Table 1 (Burns, 1993; Cudahy and Ramanaidou, 1997; Laukamp et al., 2021 and references therein).

We mapped the distribution of (1) epidote and chlorite, (2) white mica, (3) kaolinite, (4) pyrophyllite, (5) alunite, and (6) Fe oxides and hydroxides. These hyperspectral mineral maps were lately interpreted as "alteration zones" following the hydrothermal and supergene alteration models available for the study areas. The presence/absence of a distinctive absorption feature was highlighted using a multiple feature extraction workflow and thresholds in order to separate each mineralogical phase. Table 2 provides the expression for each index, constructed using band combinations and ratios for mapping several target minerals based on their diagnostic spectral feature. A detailed description of the spectral indexes construction and minimum thresholds definition is provided in the Appendix, together with the high-resolution electronic versions of the PRISMA spectral mineral maps.

The hyperspectral mineral mapping performances are assessed by building up ROIs on PRISMA imagery over selected areas where the target alteration mineral is defined by the PRISMA-derived mineral mapping. The spectra were, then, compared to the USGS reference spectra (Kokaly et al., 2017b) representative of each target phase downsampled to the PRISMA hyperspectral resolution after continuum removal to normalize the spectra.

4. Results

4.1. PRISMA mineral maps

4.1.1. The Río Blanco-Los Bronces Porphyry Cu-Mo district

Fig. 4 reports the results of the spectral mapping obtained by means of the feature-extraction band ratios proposed in this study. In Fig. 4a the areas characterized by the presence of the Al-OH feature at 2200 nm, corresponding to Al-sheetsilicates, such as white micas, kaolinite and smectites, are displayed with increasing relative abundance represented by a gradient from blue to red colors.

The zones defined by deeper 2200 nm feature (in yellow to red colors), which mean higher relative abundances, occur over a wide area in correspondence of the major mineralized deposits at Ortiga, Los Sulfatos and Río Blanco-Los Bronces (Fig. 1b), as well as in other minor areas in the northern and the eastern portions covered by the PRISMA image. As illustrated in Fig. 4b, pixels characterized by the presence of the 2250 nm feature, corresponding to the association chlorite + epidote, are distributed in several zones over the entire area covered by PRISMA, generally appearing as outer rims of the areas outlined in the 2200D map (Fig. 4a). Well defined geometries mainly occur in the Los Sulfatos area, as well as in distal areas north and south from Ortiga. Both areas were better characterized by applying the 2200W, the 2160D and the 1480D indices (Figs. 4c, d and e), which describe the wavelength shift of the 2200 nm feature and the depth of the 2160 nm and the 1480 nm absorptions, respectively. The former, shown in Fig. 4c, defines a concentric pattern ranging from lower values (blue colors) in the center – indicating Al-rich sheetsilicates characterized by the feature at around 2191–2199 nm – evolving to higher values (from green, yellow to red colors) in the outer zones – due to the absorption occurring at around 2199–2206 nm.

The highest values of the 2160D index (red colors in Fig. 4d) suggest that the Ortiga area is predominantly composed of kaolinite and alunite, both defined by a characteristic doublet consisting of a major feature at around 2206 nm related to a minor feature at 2160 nm and 2170 nm, respectively. Based on the 1480D index results, some areas are characterized by higher relative abundances of alunite (red colors in Fig. 4e). On the contrary, the absence of the feature at 2160 nm at Los Sulfatos (except for very limited areas; Figs. 4d and 5), suggests that white micas are the main Al-sheetsilicates composing the altered rocks of the area. White micas in the Los Sulfatos area evolve from Al-rich (i.e., muscovite) in proximity of the main orebody to Al-poor white micas (or Al-rich

Table 1
VNIR electronic processes and SWIR 2-active vibrational modes typically observed in rock-forming and alteration minerals and their wavelength positions (expressed in nm).

Mineral Group	Mineral Species	Assignment of Absorption	Wavelength (nm)		References
			Lower Limit (nm)	Upper Limit (nm)	
di-oct. sheet silicate	muscovite, phengite, paragonite	$\nu + \delta$ (M)2OH	2185 ([VI]Al-rich)	2215 ([VI]Al-poor)	(Vedder and McDonald, 1963)
	kaolin group	$\nu + \delta$ M2OH$_o$	2159		(Frost and Johansson, 1998)
		$\nu + \delta$ M2OHi	2209		
	pyrophyllite	$\nu + \delta$ M$_n$OH	2166		(Zhang et al., 2005)
sulfate	alunite	2νM$_n$OH, $\nu + 2\delta$H$_2$O	1473 (K-rich)	1491 (Na-rich)	(Bishop and Murad, 2005)
		$\nu + 2\delta$M$_n$OH	1762 (Na-rich)	1764 (K-rich)	(Bishop and Murad, 2005, Chang et al., 2011)
		$\nu + \delta$ M$_n$OH	2172		(Bishop and Murad, 2005)
sulfate	jarosite	2νM$_n$OH, $\nu + 2\delta$H2O	1471		(Bishop and Murad, 2005)
tri-oct. sheet silicate	clinochlore, chamosite, ripidolite	$\nu + \delta$ M2OH	2248 (Mg-rich)	2261 (Fe^{2+}-rich)	(McLeod et al., 1987; Bishop et al., 2008)
sorosilicate	epidote group	$\nu + \delta$ M$_n$OH	2250		(White et al., 2017)
Fe-oxides and hydroxides	goethite, hematite, jarosite	CFA	870 (hematite)	930 (goethite), 910 (jarosite)	(Cudahy and Ramanaidou, 1997; Crowley et al., 2003)

Notes: Lower and upper wavelength positions only given for absorption bands where related compositional changes are discussed in this study (see Laukamp et al., 2021 and references therein for further details).

Table 2
Band ratios used for extracting the relative intensity and wavelength position of the target minerals' absorption features. Method based on Laukamp (2022).

Mineral	Abundance (intensity) band ratio	Composition (wavelength) band ratio	PRISMA depth (intensity) band ratio	PRISMA wavelength band ratio	Lower stretching limit	Upper stretching limit	Masks
Fe (oxyhydr-) oxides abundance (FOA)	900D		(B44 + $B17_{SWIR}$)/ B57		2.16	2.20	
Al-sheetsilicates	2200D		(B126 + B135)/ B131		2.05	from 2.10 to 2.23	
Al-sheetsilicate		2200W		(B129/B133)	0.93	1.04	2200D > 2.054
Chlorite + Epidote	2250D		(B134 + B139)/ B137		2.05	2.10	
Kaolin group	2160D		(B123 + B131)/ B126		from 2.025 to 2.05	2.13	
Kaolinite-Alunite/ Pyrophyllite		2160W		B125/B126	0.95	1.05	2160D > 2.025
Alunite/Jarosite	1480D		(B51 + B56)/B52		2.25	2.30	2160D > 2.025–2.05 (for alunite) 900D > 2.16 (for jarosite)
Alunite		1480W		B52/B53	0.89	0.93	2160D > 2.025 1480D > 2.26
Alunite	1760D		(B76 + B82)/B80		2.18	2.20	2200D > 2.054 2160D > 2.025

phengite; defined by a feature centered at 2199–2206 nm) in distal areas. As shown in Fig. 5, the Los Sulfatos deposit area is characterized by zoned geometry consisting of local concentric pattern that is defined predominantly by Al-rich white micas (~1 km wide zone) in the center, and, to a letter extent, by kaolinite(+alunite) (few pixels), followed by a concentric outer zone (~500 m wide) of moderate-wavelength white mica, and then a more distal (~2 km away) chlorite + epidote zone exposed (at least 1 km wide) on at one side (west) of the white mica proximal alteration zonation.

However, the precise spatial pattern of the alteration zonation in this area is compromised by extensive transported cover and/or deep shade at the time of satellite image acquisition. The Ortiga area, instead, is defined by a widespread zone with kaolinite and alunite mixture (2160–2170 nm) with locally higher alunite contents (1480 nm), evolving to variably extended white micas and chlorite + epidote alteration zones – determining a zoned NW-SE trending alteration halo covering over 200 km^2 (Fig. 4). The Río Blanco deposit area, although partially covered by alluvial and/or colluvial sediments, is typified by high relative abundances of Al-sheetsilicates, consisting mainly of white mica and/or Al-rich phengite as indicated by the 2200W compositional index, whose values shift from intermediate compositions towards the Al-poor end-member (pixels from green to red colors, Fig. 4c). The kaolinite and alunite phases are absent in the surrounding area of this deposit, as indicated by the 2160D, as their values do not exceed the lower threshold, except for a spot ~ 3 km SE of the main Río Blanco deposit, surrounded in the outer zone by high values of Al-poor white mica (Fig. 4d). In the same area, only a few pixels, towards the northeast and southwest, are characterized by high relative abundance values of chlorite and epidote (Fig. 4b).

4.1.2. The Marimaca district

In Fig. 6a, red colors correspond to areas characterized by high 2200D values, which refer to relatively higher abundances of Al-sheetsilicates (white micas and/or kaolin group minerals). The outlined pixels extend over a wide area of more than 30 km^2, occurring in correspondence with the known Cu-mineralization occurrences. The zone grades west- to southward to areas characterized by chlorite + epidote relatively higher abundances as indicated by pixels with high 2250D values (red colors in Fig. 6b).

The two defined areas are separated by a white mica + chlorite transitional zone occurring in between, which is characterized by a predominance of white mica over chlorite + epidote. In Fig. 6c, the 2200 nm wavelength-position band ratio (2200W), only performed on those pixels with 2200D values higher than the lower threshold defined, is shown. Most white micas-bearing pixels to the south of the mineralized deposit, are characterized by values higher than the established threshold of ~ 1.04 (green to red colors), thus displaying a longer Al-OH absorption wavelength position close to 2206 to 2220 nm, meaning that the Al-sheetsilicates composition varies mainly from intermediate to Al-poor white mica ("phengitic"). A small area located ca. 6 km east from the main project, hereafter "new target", is characterized by a shorter Al-OH absorption wavelength position close to 2190–2200 nm (dark blue zones in Fig. 6c), indicating that the Al-sheetsilicates composition is predominantly Al-rich (i.e., in the area white mica and kaolinite, as well as Al-rich phengite, prevail). High values of the 900D (corresponding to Fe-oxides to hydroxides relative abundances) have been revealed both in the Marimaca Copper Project area (including in the Mercedes, Roble and Cindy prospects) and in the new target area (red colors in Fig. 6d). In general, it is feasible to differentiate hematite from goethite by analyzing the shift around the 900 nm absorption feature using the Hematite-Goethite ratio. However, in this study, their discrimination was not possible. This could be due to either the pronounced mixing of these two mineral phases or the predominance of goethite at the surface. It may also be attributed to the see-saw pattern superimposed on the longer VNIR wavelength range, or it could be a combination of all these factors.

A more detailed view of the Marimaca Copper Project (Fig. 7) highlights zones with relatively high values of the 2200D ratio (corresponding to the occurrence of Al-sheetsilicates) surrounding the main mineralized area, mostly located to the east of the eastern limit of the mineralization (that is known as "hanging wall alteration front", see Kalanchey et al., 2020) (Fig. 7a).

As previously shown in Fig. 6c, these areas are characterized by intermediate to longer wavelength white micas, occurring in spots east of the Marimaca Copper Project areas (green to yellow colors), likely indicating a more phengitic composition. On the contrary, higher values of the 2250D index mainly characterize sporadic but widespread portions ("haloes") to the west of the main mineralized area (Fig. 7b). Relatively higher abundances of ferric iron (oxy-) hydroxides (Fig. 7c) characterize the central portion of the Marimaca Copper Project, including the Marimaca deposits and the other minor prospects (from north to south Cindy, Roble, Mercedes, Tarso and Sierra; Fig. 2b). In Fig. 7d, the results regarding the 1480 nm feature depth index (1480D), only performed on selected pixels with high 900D, are shown. The areas corresponding to the Roble, Cindy and Emilia prospects are characterized by higher 1480D values, indicating higher relative abundances of jarosite in those areas compared to the Marimaca Copper Project zone. The linear, NNE-trending arrangement of high pixels with high (red)

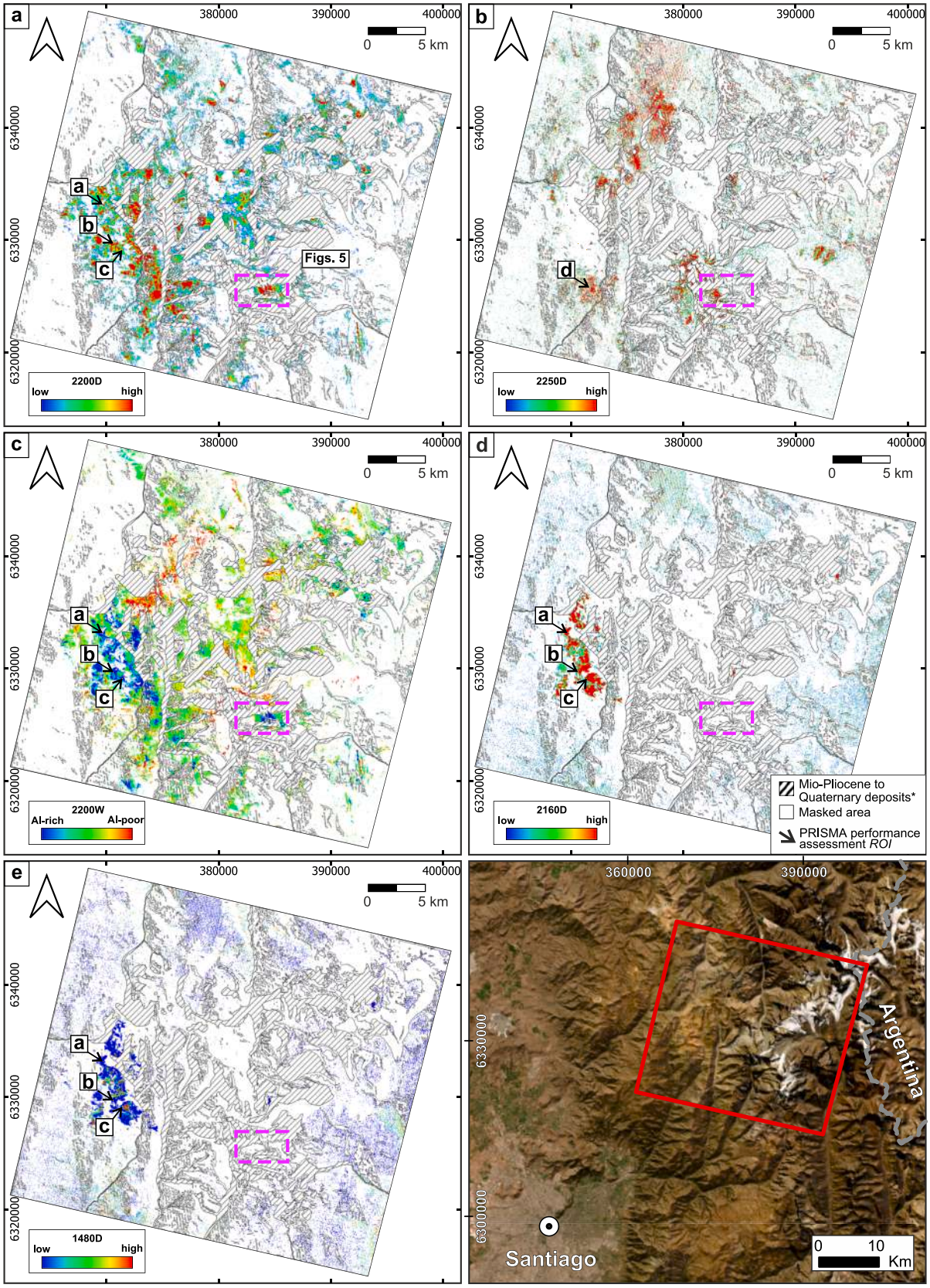

(caption on next page)

Fig. 4. Mineral maps of feature-based spectral indices applied to the PRISMA L2C scene of the Río Blanco-Los Bronces district: (a) 2200 nm feature depth (2200D) map, minimum threshold value at 2.05; (b) 2250 nm feature depth (2250D) map, minimum threshold at 2.05; (c) 2200 nm feature wavelength (2200W) map, masked for 2200D > 2.05; (d) Kaolin group relative abundance (2160D) map, minimum threshold value at ~ 2.03; (e) Alunite relative abundance (1480D) map, masked for 2160D>~2.03. D is the depth (intensity) of the spectral absorption feature (i.e., relative abundance), W is the wavelength position (i.e., composition). All the maps are masked for Miocene – Quaternary alluvium and colluvium deposits, indicated as white areas with black stripes. The white areas indicate the pixels masked out for the terrain shadows, the occurrence of vegetational and snow cover, as well as areas where the relative abundance does not exceed the minimum threshold value. Dashed purple boxes show the location of Fig. 5. Lower-case letters indicate the corresponding PRISMA spectrum in Fig. 9. The box in the bottom right corner shows the position of the PRISMA imagery. Background World Imagery data sources: Esri, Maxar, GeoEye, Earthstar Geographics, CNES/Airbus DS, USDA, AeroGRID, ING, and the GIS User Community. *Data from Toro et al. (2012). (For interpretation of the references to colour in this figure legend, the reader is referred to the web version of this article.)

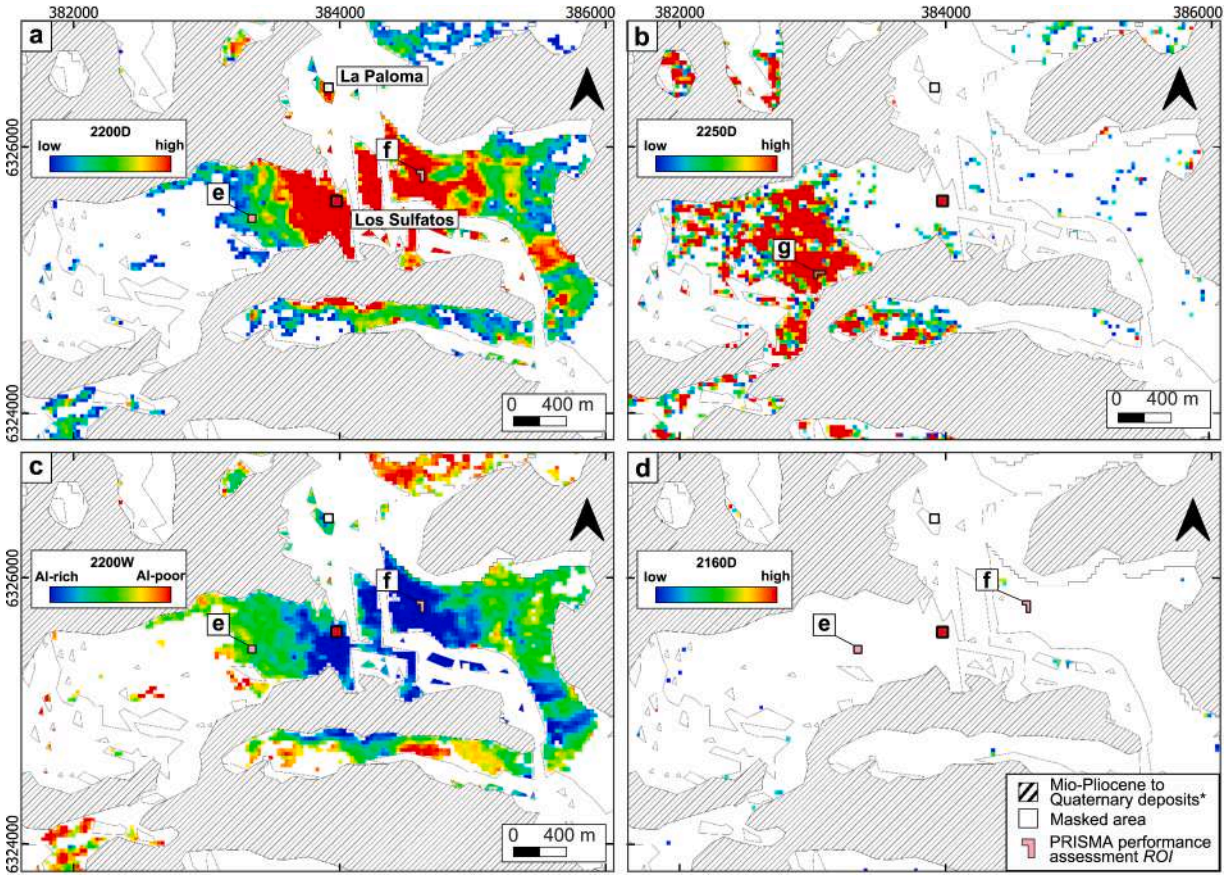

Fig. 5. Magnified mineral maps of feature-based spectral indices applied to the PRISMA L2C scene of the Los Sulfatos deposit area: (a) 2200 nm feature depth (2200D) map, minimum threshold value at 2.05; (b) 2250 nm feature depth (2250D) map, minimum threshold at 2.05; (c) 2200 nm feature wavelength (2200W) map, masked for 2200D > 2.05; (d) Kaolin group relative abundance (2160D) map, minimum threshold value at ~ 2.03. All the maps are masked for Miocene – Quaternary alluvium and colluvium deposits, indicated as white areas with black stripes. The white areas indicate the pixels masked out for the terrain shadows, the occurrence of vegetational and snow cover, as well as areas where the relative abundance does not exceed the minimum threshold value. Lower-case letters indicate the corresponding PRISMA spectrum in Fig. 9. *Data from Toro et al. (2012).

1480D values can be ascribed to instrument striping and does not represent a geological feature.

Fig. 8 shows in more detail mineral maps corresponding to the 2200D, 2250D, 2160D, 2160W, 2200W, 1480D, 1760D, 1480W and 900D ratios, which can be used for vectoring towards the so-called "new target" occurring just a few kilometers (~6 km) east from the Marimaca Copper Project. The area is characterized by a circular zoned pattern highlighted by high 2200D values (Al-sheetsilicates relative abundances; Fig. 8a). To the east, the area is characterized by higher 2250D values, suggesting the presence of distal chlorite + epidote (Fig. 8b). The 2160D map (kaolin group minerals abundances and pyrophyllite/alunite; Fig. 8c) reports higher values in the center of the area. As shown by the 2160W map in Fig. 8d, a shift to longer wavelengths (~2167–2170 nm) is recorded in the core zone of the area, potentially corresponding to a higher amount of either alunite or pyrophyllite (+alunite), which are both characterized by broad absorption features at around 2160 nm (2172 and 2166 nm, respectively), whereas lower 2160W values occurring in pixels along the rims of the body suggest a greater relative abundance of kaolinite (for which one of the diagnostic spectral feature occurs at shorter wavelength, i.e. 2159 nm). The analysis of the wavelength position of the Al-OH absorption feature is shown in the 2200W map in Fig. 8e. The PRISMA-derived map displays very low 2200W values at the center of the ore body, suggesting occurrence of kaolinite and Al-rich white mica. The varying position of the feature at around 2200 nm, which from the core zone outwards shifts to longer wavelengths (from 2199 to 2214 nm), evidences a varying composition grading outward to an Al-poor ("phengitic") white mica.

Both the features at ~ 1480 nm and ~ 1760 nm, characterize alunite (Tab. 1). The wavelength position of the OH + H_2O-related alunite absorption feature is shown in the 1480W map in Fig. 8h. The results show

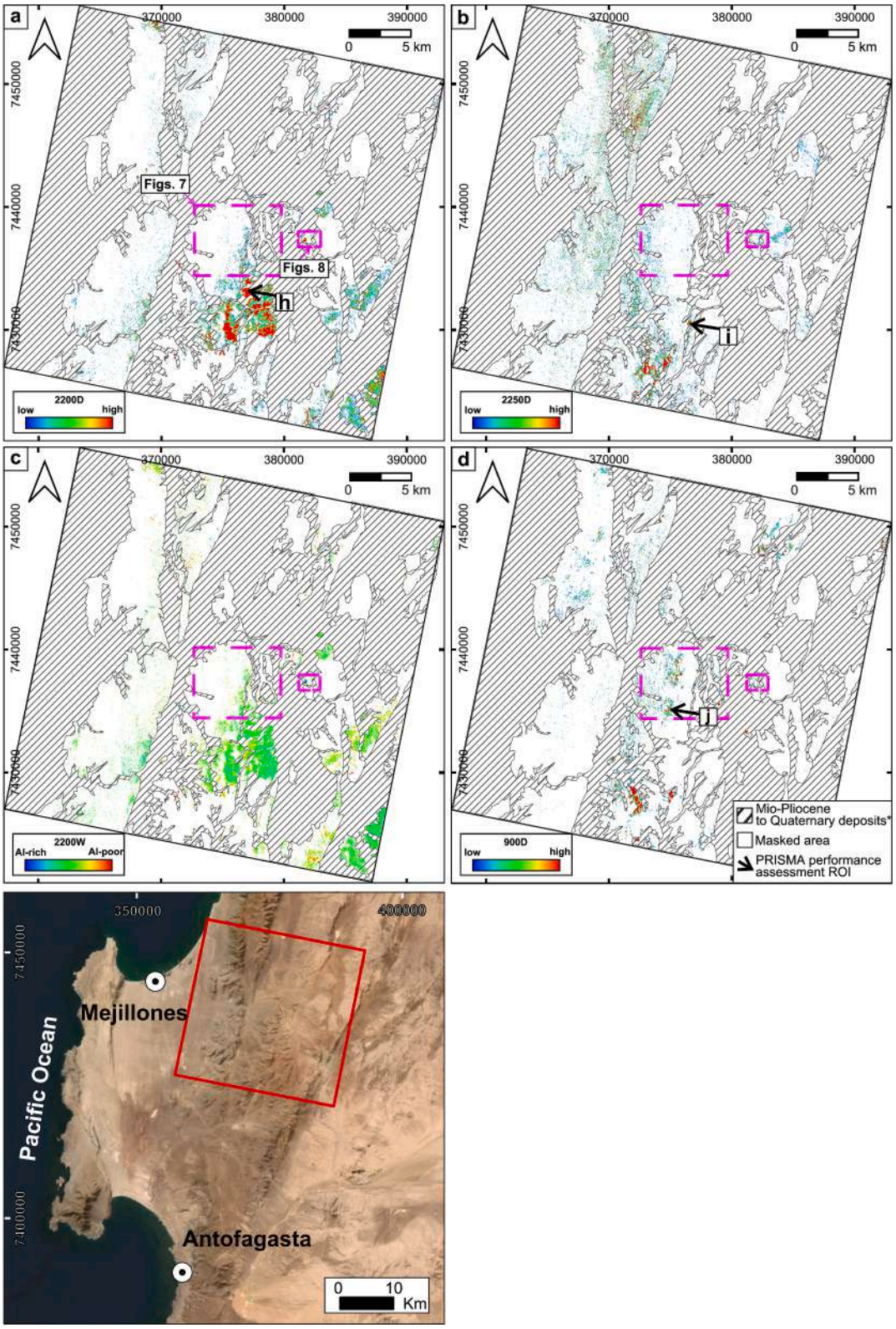

Fig. 6. PRISMA-derived mineral maps of the Marimaca Project area, obtained by applying the feature-based spectral indices; (a) 2200 nm feature depth (2200D) map, minimum threshold value at 2.05; (b) 2250 nm feature depth (2250D) map, minimum threshold value at 2.05; (c) 2200 nm feature wavelength (2200W) map, masked for 2200D > 2.05; (d) Ferric Oxides Abundance (900D) map, minimum threshold at 2.16. All the maps are masked for Mio-Pliocene to Quaternary deposits, indicated as white areas with black stripes. The white areas indicate the pixels masked out for the terrain shadows and the vegetational cover, as well as areas where the relative abundance does not exceed the minimum threshold value. Dashed purple boxes refer to the main areas of interests (magnifications in Figs. 7 and 8). Lower-case letters indicate the corresponding PRISMA spectrum in Fig. 9. The box in the bottom left corner shows the position of the PRISMA imagery. Background World Imagery data sources: Esri, Maxar, GeoEye, Earthstar Geographics, CNES/Airbus DS, USDA, AeroGRID, ING, and the GIS User Community. *Data from Cortés et al. (2007). (For interpretation of the references to colour in this figure legend, the reader is referred to the web version of this article.)

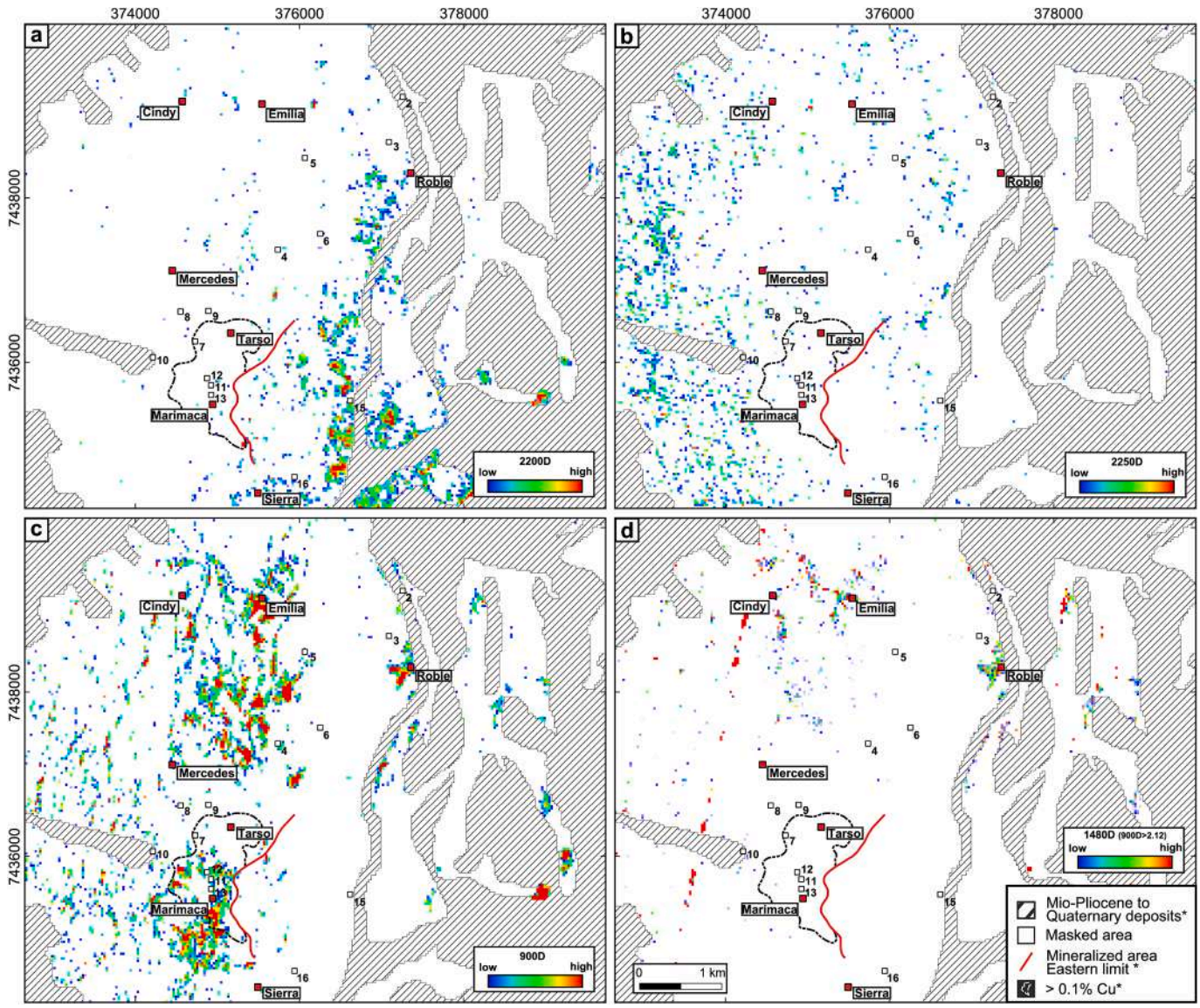

Fig. 7. Magnified PRISMA-derived mineral maps on the main mineralized area of the Marimaca Project, obtained by applying the feature-based band ratios; (a) 2200 nm feature depth (2200D) map, minimum threshold value at 2.05; (b) 2250 nm feature depth (2250D) map, minimum threshold value at 2.05; (c) Ferric Oxides Abundance (900D) map, minimum threshold value at 2.16; (d) Jarosite relative abundance (1480D) map, masked for 900D > 2.16. All the maps are masked for Mio-Pliocene to Quaternary deposits, indicated as white areas with black stripes. The white areas indicate the pixels masked out for the terrain shadows and the vegetational cover, as well as areas where the relative abundance does not exceed the minimum threshold value. Deposit number is reported in Cortés et al. (2007). *Data from Cortés et al. (2007); Kalanchey et al. (2020); Oviedo (2017, 2022).

higher values in the core zone, corresponding to Na-rich alunite characterized by the main feature shifted at longer wavelength at~ 1491 nm, compared to the rims (1480 nm). The area is widely characterized by high 900D values (Fig. 8i), with highest values in correspondence of the main kaolinite/alunite-bearing zone and of the areas with higher 2200D (Al-poor white mica-muscovite) and 2250D values (Figs. 8a to h).

4.2. *Evaluation of the PRISMA performances through the analysis of the spectra*

The spectra derived from the selected ROIs (in black dotted lines), created on the investigated PRISMA L2C VNIR-SWIR scenes are reported in Fig. 9 and compared with USGS spectral library spectra of the target minerals (version 7; Kokaly et al., 2017b). Most of the PRISMA spectral signatures look very similar and consistent with the USGS spectral library. In the PRISMA spectra deriving from high-2200D ROIs (e.g., Figs. 9e and g), the main absorption feature of Al-sheetsilicates ($\nu + \delta$(M)2OH at ~ 2200 nm) appears well defined; although smaller, the same feature is well visible also in ROIs containing other minerals, like chlorite and epidote (e.g., Fig. 9k), indicating a complex assemblage of alteration minerals. Moreover, as shown in Fig. 9e the displacement of the center of the 2200 nm feature, from 2191 to 2200 nm, is well visible at the PRISMA resolution. The chlorite and epidote main spectral absorption feature ($\nu + \delta M_nOH$ at ~ 2250 nm) is also sharp (Figs. 9d, f, h, j and k) accompanied by a feature at ~ 2340 nm, and a deepening of the absorption is shown by the spectra in Figs. 9d and h, referring to the ROIs collected in the areas with highest 2250D values (see Figs. 4 and 6b).

A shallower feature is shown in the ROIs *g*, *k* and *l* (Figs. 9f, j and k) collected in the Los Sulfatos and the new target areas (Figs. 5b and 8b). The spectrum *l*, moreover, defines an area characterized by a mixture of white mica and chlorite, as both the features at 2200 nm and 2250 nm are present. The ROIs picked up in the areas characterized by high values of the 2160D band ratio (Figs. 4d, 8c and d), report spectral

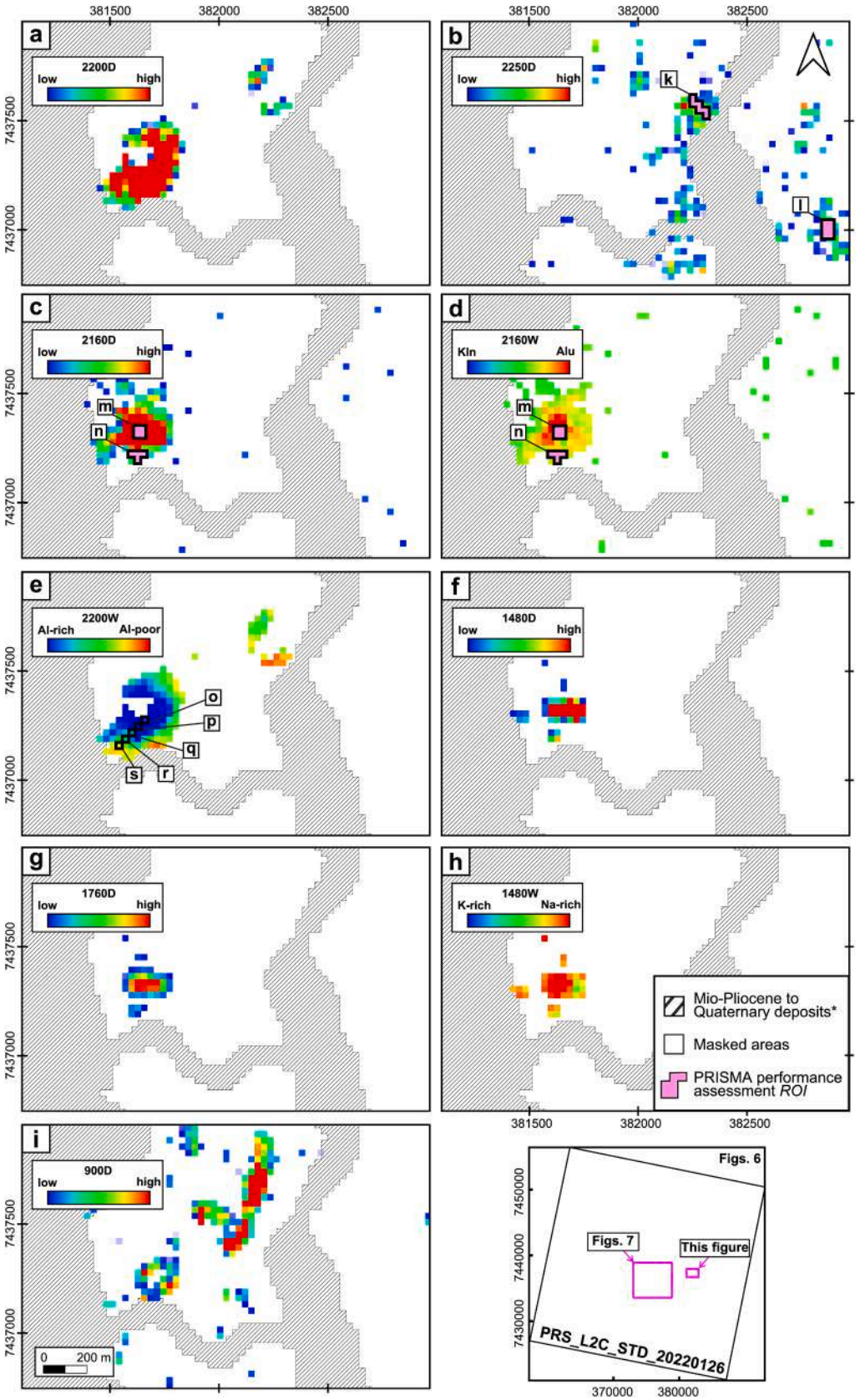

(caption on next page)

Fig. 8. Magnified PRISMA-derived mineral maps on the new target area obtained by applying the feature-based band ratios; (a) 2200 nm feature depth (2200D) map, minimum threshold value at 2.05; (b) 2250 nm feature depth (2250D) map, minimum threshold value at 2.05; (c) 2160 nm feature depth (2160D) map, minimum threshold value at ~ 2.03; (d) Kaolinite-alunite compositional variation based on the position of the absorption feature between 2159 nm (kaolinite) and 2167 nm (alunite) (2160W), masked for 2160D>~2.03; (e) 2200 nm feature wavelength (2200W) map showing the wavelength shifting around the 2200 nm feature (2191 nm to 2214 nm) meaning the presence of Al-rich (white mica, kaolinite) and Al-poor (phengite) sheetsilicates, masked for 2200D > 2.05; (f) 1480 nm feature depth (1480D) map, masked for 2160D>~2.03; (g) 1760 nm feature depth (1760D) map, masked for 2160D>~2.03; (h) Alunite compositional variation based on the 1480 nm wavelength (1480W) map, masked for 1480D > 2.25; (i) Ferric Oxides Abundance (900D) map, minimum threshold value at 2.16. Lower-case letters and black boxes (from o to s) indicate the corresponding ROIs-derived PRISMA spectrum in Fig. 12. Lower-case letters and pink boxes indicate the corresponding 6-pixels-ROI-derived PRISMA spectrum in Figs. 9d-n. All the maps are masked for Mio-Pliocene to Quaternary deposits, indicated as white areas with black stripes. The white areas indicate the pixels masked out for the terrain shadows and the vegetational cover, as well as areas where the relative abundance does not exceed the minimum threshold value. *Data from Cortés et al. (2007). (For interpretation of the references to colour in this figure legend, the reader is referred to the web version of this article.)

signatures comparable to those of kaolinite and/or alunite (Figs. 9a, b, c, l and m). The characteristic doublet absorption features fixed at ~ 2160 and ~ 2209 nm ($\nu + \delta$ Al_2OH_o and $\nu + \delta$ Al_2OH_i, respectively) are well represented in the PRISMA-derived spectra, accompanied by combination bands typical of kaolin group minerals, located at around 2330 nm and 2380 nm (Figs. 9b and m). Moreover, differently from the spectra in Fig. 9a collected in the Ortiga area, a shift to longer wavelengths (~2167–2170 nm) characterizes the center of the system for the new target area, potentially dominated by alunite, as displayed by the alunite spectral signature in Fig. 9l, as already shown in the 2160W, 1480D and 1760D maps in Figs. 8d, f and g. Finally, the spectrum collected in the areas characterized by high Fe-oxides and hydroxides relative abundances, resulting from the application of the band ratio (900D) in the Marimaca Copper Project, were plotted against the spectral signatures of gossan. Both the CTS and CFA features (at ~ 500 and 910 nm) related to the presence of Fe-hydroxides (goethite) are well represented in the PRISMA-derived spectra. Although very shallow, the Fe^{3+} 908 nm absorption feature (band 57 of the PRISMA VNIR cube), is quite well represented in the PRISMA-derived spectrum in Fig. 9i.

5. Discussion

5.1. Interpretation of the hydrothermal alteration footprint related to IOCG and porphyry-Cu(-Mo) mineral occurrences derived from PRISMA mineral maps

The Andean IOCGs and porphyry Cu(-Mo) deposits are distinct mineral systems and not genetically related (Pollard, 2000; Lang and Thompson, 2001; Sillitoe, 2003): the former are Fe-oxide rich (predominantly hematite and magnetite), and have volumetrically extensive high-temperature alteration zones in which the fluid migration requires a significant physicochemical gradient, especially in terms of REDOX conditions, whereas, the latter are Fe-sulfide rich and have narrower high-temperature alteration zones. Nonetheless, the PRISMA results presented here show in both the deposit types the occurrence of wide alteration zones, with distinct mineral patterns, directly related to the magmatic-hydrothermal genesis (Barra et al., 2017). This is an important point in the frame of remote sensing-based mineral exploration, because: (1) the similar genetic conditions could allow a comparison between these two deposit types in terms of alteration mineral assemblages and zones; (2) the presence of large-scale alteration features is crucial for satellite remote sensing application and district-scale exploration, since available spaceborne sensors are commonly characterized by a spatial resolution of around 30 m, and (3) the alteration minerals characterizing the aforementioned zones (e.g., white micas, kaolin group minerals, sulfates - like alunite, chlorite, epidote and biotite) are very well characterized over the SWIR wavelength region (around 2200, 2160 and 2170, and 2250 nm, respectively).

It is known that remote sensing investigations require to be validated through field data. Thus, in order to test the performances of PRISMA in mineral mapping, we used detailed field-derived data from literature and technical reports for supporting the remote-based interpretations. For discriminating between the two deposit-types directly through interpretation of remote sensing over unknown areas it could be considered that the mineralization and the alteration characterizing the porphyry-Cu systems are generally confined to cylindrical porphyry stocks, whereas IOCGs have less focused alteration footprints, with haloes that could extend for several kilometers in association with second- to lower-order splays of major faults zones, intrusive contacts, or permeable stratigraphic layers, (Meyer et al., 2022). Sulfur-poor IOCG systems are commonly characterized by the absence of acidic alteration minerals (like alunite) and show a more widespread occurrence of sericite and chlorite (Kreiner and Barton, 2017).

5.1.1. The Río Blanco-Los Bronces district

In the Río Blanco-Los Bronces district, alteration zones characterized by distinct occurrence of alunite-kaolinte, sericite, biotite, chlorite-epidote, have been already documented and mapped (Irarrazaval et al., 2010; Toro et al., 2012), providing useful information for validating the satellite hyperspectral data. In the PRISMA district map, the Al-OH 2200 nm feature (2200D) is highlighted in a large zone where the San Francisco batholith outcrops (Fig. 4a). High 2200D values discriminate areas with relatively higher abundances of Al-sheetsilicates, such as white mica, kaolin group minerals and/or Al-smectite, which are characterized by the presence of a distinct spectral feature at 2200 nm. In order to better discriminate alteration minerals assemblages and zones, a lower threshold of 2.05 for the 2200D index was defined, then the 2200 nm feature (2200W) composition band ratio (Fig. 4c) was applied to distinguish Al-rich white mica and kaolinite-bearing areas from Al-poor white micas (phengite) and Al-smectite. The information extracted from these two indices and from the identification of the area characterized by the presence of the 2160 nm feature (kaolin group and alunite relative abundances; Fig. 4d) enabled to outline areas where the latter minerals outcrop, guiding the interpretation of the alteration zones distribution (Figs. 10a and b).

More specifically, it was possible to discriminate areas with white micas (feature at 2200 nm but not at around 2160 nm) from kaolinite- and alunite-rich zones (both feature at 2200 nm and 2160–2175 nm, characterized by variable intensities), corresponding in this case to the sericitic and advanced argillic alteration alteration zones, respectively (Irarrazaval et al., 2010; Toro et al., 2012). Looking in detail at the Los Sulfatos area (enlarged map in Fig. 5), the results obtained show that the white mica characterizing the sericitic alteration halo exhibits a displacement of the position of the absorption at 2200 nm, from 2191 nm in the proximity of the center to 2199 nm outward (Fig. 5c). Several authors have outlined that variation in white mica composition can reflect either alteration type or intensity, or fluid geochemistry, as well as it can be a proxy for the occurrence of high-grade ores (van Ruitenbeek et al., 2005; Harraden et al., 2013; Tappert et al., 2013; Halley et al., 2015; Meyer et al., 2022). The wavelength position of this feature is mainly controlled by the Tschermak exchange ($Al^{IV}Al^{VI}Si^{IV}_{-1}(Mg,Fe)^{VI}_{-1}$; Velde, 1965; Duke, 1994), which is also controlled by pH (Wang et al., 2017). This considered, the highlighted Tschermak exchange could suggest the evolution from the more acidic and high-temperature alteration mineral core zone to the distal lower-temperature neutral to acidic alteration mineral zone. Looking at the existing data in the Los

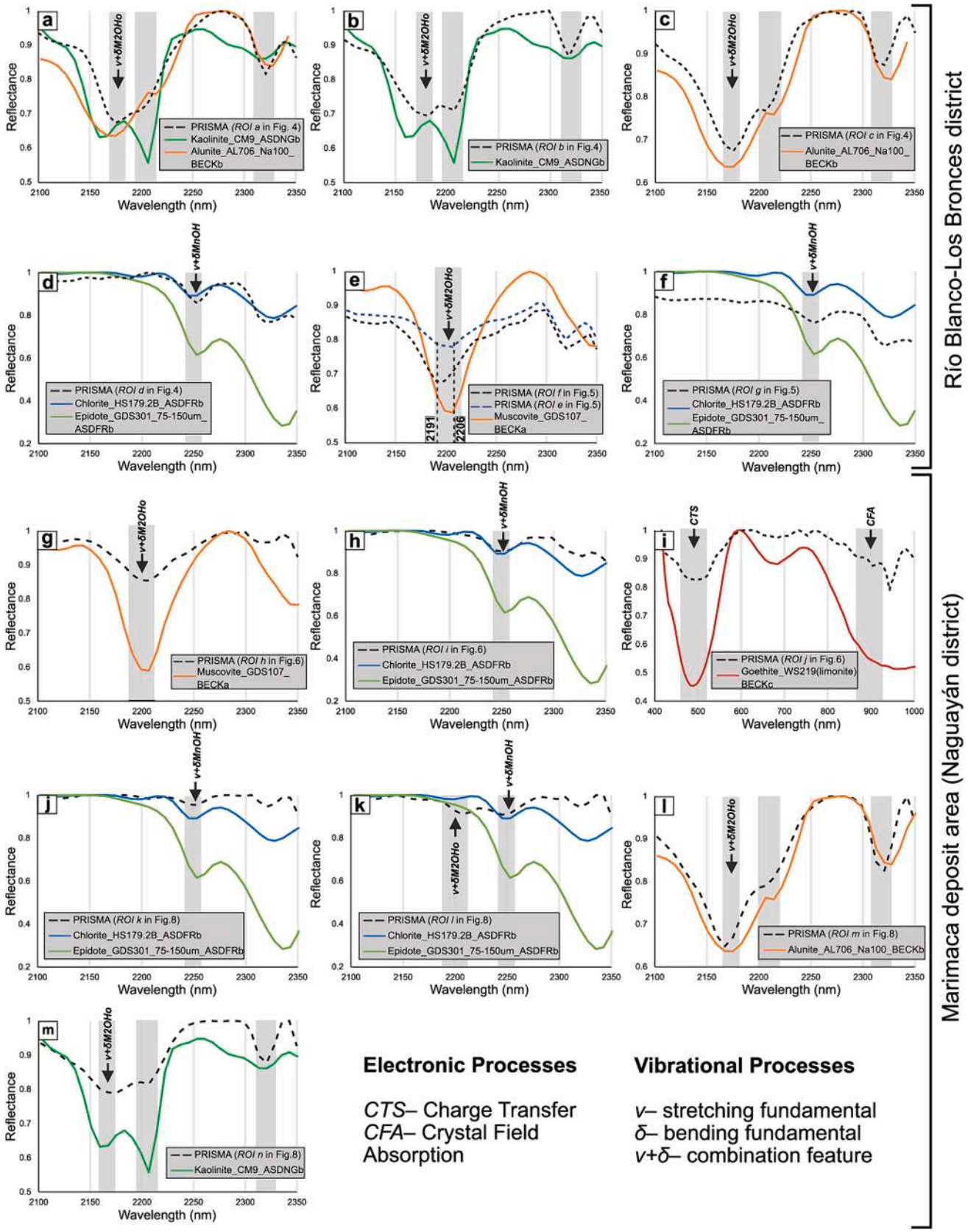

Fig. 9. Comparison between USGS representative spectra (Kokaly et al., 2017b) and PRISMA-derived L2C spectra (see Figs. from 4 and 8 for the location of the pixels indicated with lowercase letters). The respective assignment of each absorption feature (electronic and vibrational processes) is indicated.

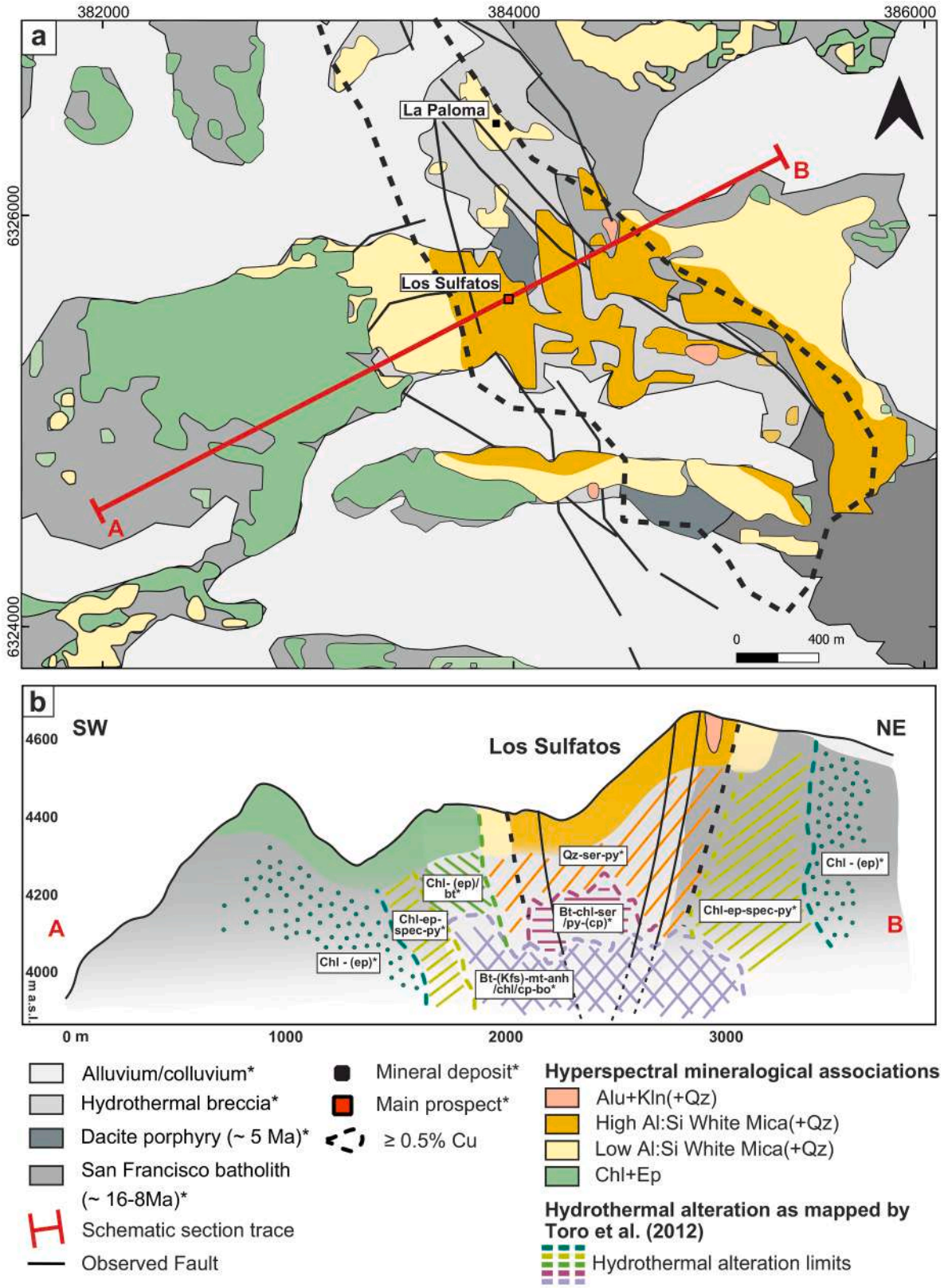

Fig. 10. (a) Geological mapping of the hyperspectral mineralogical associations resulting from the band depth and wavelength ratios applied to the PRISMA L2C scene of the Sulfatos area; (b) Schematic section crossing the main mineralized area, on which is reported our interpretation of the distribution of hyperspectral alteration minerals in depth compared with the alteration section reported by Toro et al. (2012). *Data from Toro et al. (2012). Mineral abbreviations: Anh = anhydrite; Bo = bornite; Bt = biotite; Chl = chlorite; Cp = chalcopyrite; Ep = epidote; Kfs = K-feldspar; Gy = gypsum; Mt = magnetite; Py = pyrite; Qz = quartz; Ser = sericite; Spec = specularite.

Sulfatos area (Toro et al., 2012), we see that the results are coherent with the mapped alteration zones and that the area characterized by white mica absorption feature at 2191 nm perfectly fits with the contour of the modeled mineralization (dotted line with ≥ 0.5 % Cu in Fig. 10).

Even in the proximity of the Río Blanco deposit, areas with high relative abundance of Al-sheetsilicates have been identified, primarily characterized by an intermediate to Al-rich composition (feature position at around 2206 nm), suggesting the occurrence of sericite.

The intensity of the 2250 nm absorption feature (2250D band ratio) was used for detecting the chlorite-epidote-bearing rocks, in this case mapped as characteristic for propylitic alteration zone (Irarrazaval et al., 2010; Toro et al., 2012). The higher 2250D values are mainly concentrated in zones surrounding the reported deposits and in the NNW portion of the entire investigated area (Figs. 1b, 4 and 5). Toro et al. (2012) describe strong and widespread Na-Ca-Fe metasomatism (actinolite-tremolite-scapolite-chlorite-epidote-apatite-biotite and local pyrite-chalcopyrite) affecting the volcanic and intrusive rocks, as well as an assemblage of chlorite-magnetite-epidote-calcite overprinting the late-magmatic breccias at El Plomo and San Manuel in the southwestern part of the Ortiga Area. The Los Sulfatos area is bordered by alteration zones which from the center outward are composed of chlorite-(epidote)-biotite, chlorite-epidote-specularite-pyrite and chlorite-(epidote) (Irarrazaval et al., 2010; Toro et al., 2012). The PRISMA reflectance spectra, corresponding to the pixels with 2250D index higher values, show absorption features characteristic of chlorite and epidote at around 2250 nm. The bulk of the chlorite composition (chlorite Mg#) is interpreted to be intermediate Fe – Mg chlorite based on the shift of the Mg/Fe – OH bond at wavelengths ranging around ~ 2250 – 2253 nm. The presence of epidote in the area is confirmed by its minor diagnostic absorption features at around 1550 nm and 1830 nm, which are due to 2νOH (Laukamp et al., 2021). These absorption features are typically easy to separate from hydroxyl-related overtones in other minerals (e.g., chlorite) and do not overlap with atmospheric absorptions in the 1400 and 1900 nm wavelength regions (White et al., 2017). However, as observed in this study area, these minor absorption features are diluted or completely lost when epidote occurs as secondary phase in mineral mixtures with chlorite, posing a challenge for their mapping.

In zones with higher values of 2160D index results in the Ortiga area (Fig. 4d, spectra in Figs. 9a, b and c), the presence of the feature at around 2160 nm to 2170 nm refers to the presence of kaolinite and sulfates like alunite. These are common minerals occurring in the advanced argillic alteration zone of porphyry-Cu(-Mo) systems, the so-called lithocaps which can reach > 1 km in thickness if unaffected by notable erosion. The available geological map (see Fig. 1b) reports an area with a well-developed advanced argillic alteration zone (Toro et al., 2012) nearby the Ortiga deposit, validating our observations. The spectral signatures collected in the area show a mixed contribution of both kaolinite and alunite considering only the feature at ~ 2160 nm, making it challenging to clearly distinguish a zonation from the advanced argillic alteration core, dominated by alunite, evolving to kaolinite. Alunite, however, is also characterized by a strong absorption at around 1470–1480 nm (Bishop and Murad, 2005). Therefore, the 1480D index was employed for discriminating the areas where alunite is present in higher abundances compared to kaolinite (Fig. 4e). In the Los Sulfatos area, only few pixels are characterized by high values of the 2160D index, allowing the mapping of limited areas with both alunite and kaolinite (Figs. 5d and 10a). Indeed, Toro et al. (2012) describe outcropping remnants of advanced argillic in the Los Sulfatos area, occurring as veins and ledges at higher elevations (>4600 m; Fig. 10b), supporting our observations.

5.1.2. The Marimaca district

At regional scale, the most prominent feature highlighted through the mineral mapping performed using PRISMA data, is a widespread area superimposed on the granodioritic rocks of the Naguayán Plutonic Complex, characterized by the occurrence of sericite, as evidenced by high 2200D index values (Fig. 6a). As discussed above, since it can indicate either the presence of Al-rich white mica (e.g., muscovite) or Al-poor white mica (e.g., phengite) (reflectance spectrum in Fig. 9g), the index 2200W was performed for 2200D-pixel values > 2.05 (Fig. 6c). When occurring at shorter wavelengths, the former absorption position indicates the presence of muscovite, which has higher Al amounts in the octahedral site. Our results show that the white mica characterizing the studied area has the main absorption feature at around 2206 nm in proximity of the Marimaca Copper Project (Fig. 6c), while values varying from 2199 to 2206 nm are shown in a wider area occurring towards ESE, corresponding to the sericitic alteration described by several authors (e.g., Oviedo, 2017; Kalanchey et al., 2020; Oviedo, 2022) (Figs. 6a and c). Although reflectance spectroscopy can discriminate between white micas based on their aluminum content (e.g., Tappert et al., 2013; Meyer et al., 2022), in this case, the use of traditional analytical techniques on hand specimens would have been useful for confirming these observations.

In the same area, the absence of kaolin group minerals, as well as sulfates like alunite, characteristic of advanced argillic alteration, was confirmed considering the missing features at around 2160 and 2170 nm, resulting in low values of the 2160D index. The lack of these minerals typical of acidic alteration mineral facies can be explained by considering Marimaca a sulfur-poor IOGC system (Kreiner and Barton, 2017).

From our study, it results also that the hydrothermal mineral pattern, then, progresses to chlorite-sericite and/or chlorite-epidote alteration southward, as shown by the 2250D mineral map in Fig. 6b, which reports the presence of the ν + δM3OH (with M = Mg, Fe, Al) feature characteristic of chlorite and epidote. Based on our interpretation, the presence of higher 2250D values in the westernmost zone of the study area (Fig. 6b), closer to the Marimaca Project area, could suggest either chlorite-biotite alteration or chlorite-epidote in background Ca-Na regional alteration developed around the Marimaca IOCG system (Figs. 6b and 7b), as reported by the field study of Kalanchey et al. (2020). The Ca-Na regional alteration in the area is shown mainly by albite and actinolite replacing mafic minerals, however, chlorite and epidote in spots are also common (Oviedo, 2017, 2022). However, none of these minerals could be recognized in the area or separately mapped for two main reasons: (1) SWIR 2 spectral absorptions significantly overlap for these commonly co-occurring mineral groups (Laukamp et al., 2021, and references therein), such as chlorite and epidote; (2) their spectral separability can be performed at SWIR-2 longer wavelengths, i.e., at around 2320–2340 nm and between 2377 and 2390 nm, which are covered by PRISMA bands, but have not considered for processing due to their low SNR and thus resulting in noisy outputs.

Focusing on the main mineralized area (PRISMA-derived mineral maps in Fig. 7 and interpretation map in Fig. 11), the results show chlorite (+biotite + epidote) and sericite in less extended haloes surrounding the center of the deposit area, which, instead display Fe^{3+}-bearing minerals (hydroxides and sulfates – jarosite), that can be interpreted as leached cap. Looking for comparison at the field data mapped by the mining company (Kalanchey et al., 2020), the major alteration features that control the mineralization, the so-called “hanging wall” and “footwall” alteration fronts (the former indicated with a red line in Figs. 7 and 11, hereafter “eastern” and “western” mineralization limits), occur respectively, toward the top and the bottom of the parallel-fractured diorite and monzonite units and the dykes-related mineralization. Based on field and drill-core observations, the “hanging wall” front defines the eastern limit of the mineralized area and the beginning of a sericitic alteration zone in form of haloes and evolving to the east, accompanied by minor chlorite alteration (Fig. 11a). The western limit, instead, is defined mainly by actinolite-to-magnetite alteration accompanied by variable degrees of chlorite replacement (Oviedo, 2017, 2022). The latter field-based observations agree with the results obtained from the PRISMA mineral mapping performed in this study (Figs. 7 and 11). The area, in fact, is highlighted

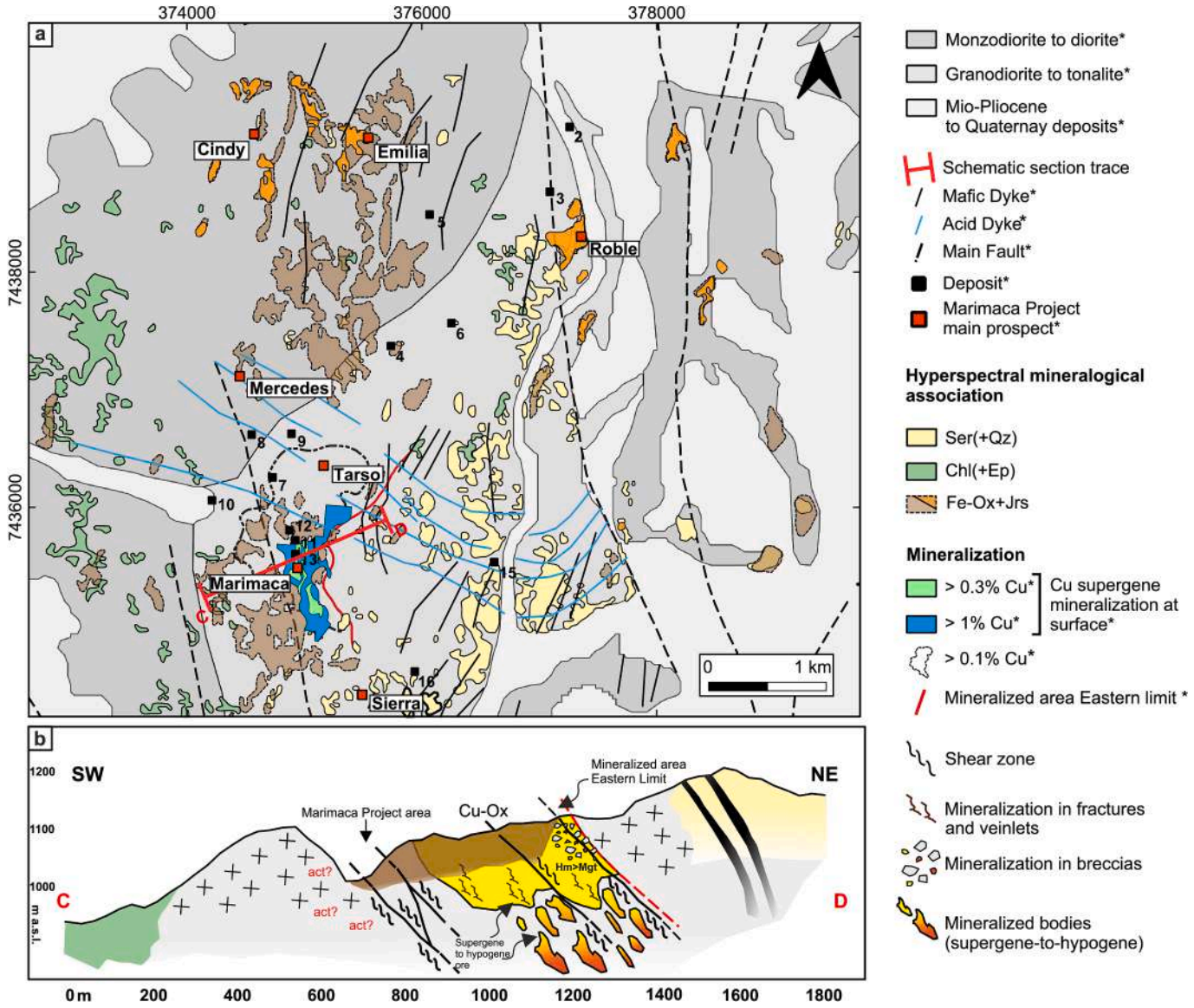

Fig. 11. (a) Geological mapping of the hyperspectral mineralogical associations resulting from the band depth and wavelength ratios applied to the PRISMA L2C scene of the Marimaca Project area. The country rocks distribution is modified from Cortés et al. (2007), deposits names indicated by numbers are reported in the notes of the geological map (Cortés et al., 2007). Mineralization distributions, the main prospects of the Marimaca Project and the mineralized area eastern limit location derive from Kalanchey et al., (2020 – NI 43 101 Marimaca Project) and Oviedo (2017). (b) Schematic section reporting the possible alteration scheme and mineralization geometry. Notes = Qz: quartz; Ser: sericite; Chl: chlorite; Ep: epidote; Fe-Ox: Fe-hydroxides; Cu: copper. *Data from Cortés et al. (2007); Kalanchey et al. (2020); Oviedo (2017, 2022).

by non-continuous zones with relatively high 2200D values towards the east of the Marimaca Project (Figs. 7a and 11) and others characterized by high 2250D index values (higher chlorite-epidote relative abundances), towards the west (Figs. 7b and 11) and in correspondence of N-to-NNE trending mafic dykes (Oviedo, 2017, 2022).

In addition, a well-developed supergene leached cap dominated by Fe^{3+}-oxy-hydroxides and sulfates (i.e., goethite, hematite, jarosite), clays and copper oxides (Kalanchey et al., 2020) was identified in the near-surface levels towards the central part of the Marimaca project area. Goethite, hematite and jarosite are also reported to occur in form of haloes in correspondence of fractures and fault zones. The PRISMA-derived mineral mapping performed by applying the 900D feature-extraction index was able to well delineate this wide supergene cap, in accordance with that reported by the mining company. At Marimaca, the Fe-Ox-bearing zones are developed mainly above the mineralized area and around the NNW-SSE trending fault reported by the Chilean Geological Survey (Cortés et al., 2007) (Figs. 7c and 11a). The same is shown in the northern part of the area of interest, mainly in correspondence of the Roble, Cindy and Emilia prospects (together with higher 2200D index values – interpreted as sericitic alteration – as well as zones of high 2250D values – implying chlorite (+epidote) alteration) (Fig. 11a). Jarosite is defined by a deep absorption feature at~ 1470 nm (Bishop and Murad, 2008; Tab. 1). The application of the 1480D index highlights areas with higher relative abundances of jarosite mainly in correspondence of the Roble and Cindy prospects (Fig. 7d), in agreement with the Marimaca Copper Corp. announcements (Marimaca Copper Corp, 2023 -https://marimaca.com/regulatory-news/), while in the Marimaca project area it appears to be composed predominantly of goethite (Fig. 7c).

All the information occurring in technical reports joined together with the ones obtained by the remote sensing approach, i.e., different combination of mineralization styles, characteristics and the location of alteration zones in the field and from satellite observation, suggest a deposit scheme likewise other IOCGs described in the Coastal Cordillera

with intermediate characteristics in-between magnetite- and hematite-rich deposits (as reported by Sillitoe, 2003; Williams et al., 2005; Chen, 2013; Barra et al., 2017, and references therein; Kreiner and Barton, 2017). The sericitic alteration represents the shallowest and the most widespread alteration facies observed in the Marimaca area. Its presence indicates either the uppermost manifestation of concealed deposits or can occur in areas proximal to orebodies. Several minor Cu-deposits are reported in the area by the Chilean Geological Survey (Cortés et al., 2007). The presence of a more prominent 2250 nm feature in some zones may refer to a higher abundance of chlorite + biotite (+epidote) and characterize the outcropping potassic alteration zone typically associated with IOCGs.

Potassic and sericite–chlorite alteration zones are typically mineralization-related (Williams et al., 2005; Chen, 2013). Chlorite + biotite(+epidote) and, locally, Ca-alteration are associated with the magnetite IOCG subtype, which is related to the earlier stages of the Cu-mineralization. In contrast, sericitic or K-feldspar-chlorite alteration is generally associated with the hematite subtype. The predominance of

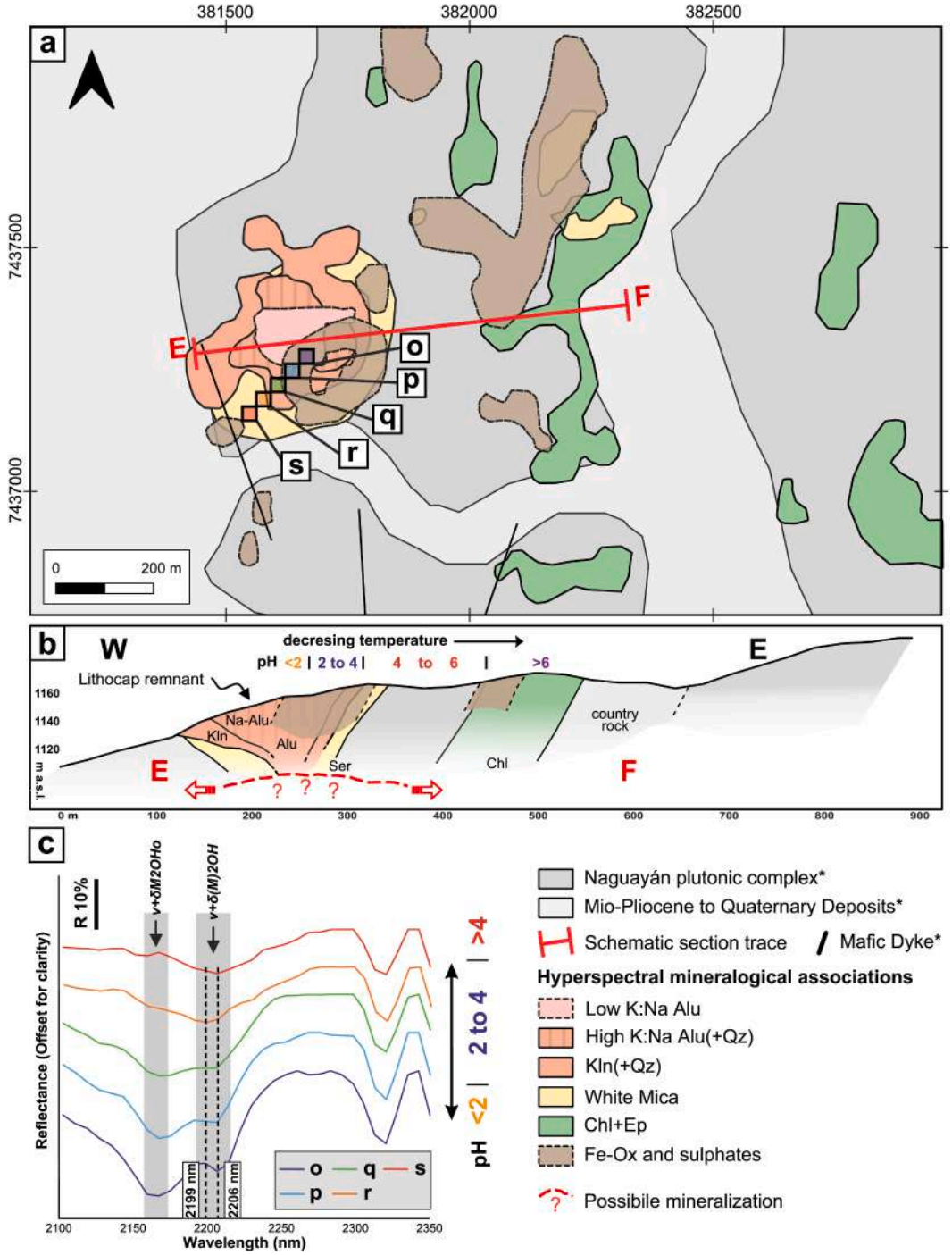

Fig. 12. (a) Geological mapping of the hyperspectral mineralogical associations resulting from the band depth and wavelength ratios applied to the PRISMA L2C scene of the new target area and location of ROIs (o to s in Fig. 8); (b) Schematic section reporting the possible alteration scheme, mineralization location and related pH values relative to alteration minerals stability (modified from Hedenquist and Arribas, 2022). Qz: quartz; Alu: alunite; Kln: kaolinite; Ser: sericite; Chl: chlorite; Ep: Epidote. *Data from Cortés et al. (2007); (c) (o-s) PRISMA-derived reflectance spectra showing the feature wavelength position moving toward of the centre of the mineral systems.

magnetite over hematite in the western limit area, nearby a potassic alteration zone (Ca-metasomatism), is described by the reports, as well as delineated by higher chlorite-biotite-epidote relative abundances in the 2250D spectral mineral maps shown in this study (Fig. 7b). At the same time, the eastern limit is described to be dominated by hematite over magnetite, nearby a sericitic alteration zone delineated also in the present study by PRISMA imagery processing. The hematite-rich IOCG types are described in literature associated with sericitic to sericitic-chloritic alteration (Chen, 2013). This outward-to-upward transition can perhaps mirror a laterally-to-vertically zoned IOCG deposit, from "deeper-intermediate" magnetite-rich to "shallower" hematite-rich facies.

New target area - Through the PRISMA hyperspectral mineral mapping, the minerals typical of advanced argillic, sericitic and propylitic hydrothermal alteration zones, were delineated in an area about 6 km east of the Marimaca Copper Project. This area, to the best of our knowledge, is not referred in any previously published reports of publications, suggesting that it may be either a minor, undervalued or a still not-identified target (Figs. 8 and 12). Moreover, minerals common in supergene leached caps covering all three hypogene alteration zones were also observed. In detail, the distribution of the mineral features results in a concentric pattern characterized by a core dominated by alunite, pyrophyllite, or alunite + pyrophyllite (red pixels in the 2160W map in Fig. 8d, and blue to red pixels in the1480D and 1760D maps in Figs. 8f and g, reflectance spectrum in Fig. 9l), surrounded by a kaolinite-dominated rim, as shown by the spectrum in Fig. 9m, characterized by a shorter wavelength position of the OH-related feature at around 2160 nm. Spectra from *o* to *q* in Fig. 12c show the predominant occurrence of kaolinite and alunite. The high content of white mica shown by the remaining edge pixels in the 2200D map (Fig. 8a) is possibly related to enhanced sericitization of feldspars of diorite to monzodiorite rocks outcropping in the area. Within the sericite zone, the white micas observed apparently register a shift of the 2200 nm absorption feature from the center outward, from ~ 2199 nm (high-Al white micas) to ~ 2206 nm (low-Al white micas) (Fig. 8e and spectra *r* and *s* in Fig. 12), likely mirroring chemical composition modifications. A more widespread area defined by high 2250D values is delineated outside of those described above, likely indicating the occurrence of sericite + chlorite. With regards to alunite, Bishop and Murad (2005) and Chang et al. (2011), described a shift to longer wavelengths of the 1480 nm feature (from around 1480 nm to 1495 nm) correlated with the increasing NaK_{-1} exchange vector. Chang et al. (2011) described alunite 1480 nm feature shifting to longer wavelengths closer to the intrusive center due to higher Na and lower K relative content in the alunite. This is related to the temperature of formation (Bishop and Murad, 2005) and, therefore, it can be used to vector towards the center of the mineralization. The variation of the 1480W index shown in Fig. 8h can therefore be interpreted in this way.

It must be pointed out that the new target area is bordered by Miocene to Quaternary alluvial-colluvial cover, which prevents satellite remote mapping further alteration in the surrounding areas, therefore, does not allow to verify the continuation of the suggested mineral zonation. In any case, the PRISMA mineral mapping of the new target area show, in plan view, a concentric alteration pattern characterized by a core dominated by Na-alunite, alunite (or pyrophyllite), coupled with a transitional (kaolinite + white mica) to a muscovite to Al-rich phengite outer rim. All of them occur above rocks perhaps characterized by sericite + chlorite and chlorite + epidote occurrence.

As pointed out by Sillitoe (2003), extensive zones of sericitic or even advanced argillic alteration may either hide buried IOCGs or suggest their presence nearby and be also associated with lithocaps overlying porphyry-Cu systems (Sillitoe, 2010). Lithocaps can be very large (>10 and locally up to 100 km^2) and wider than the underlying/related porphyry-Cu ore IOCG deposit (Sillitoe, 2003, 2010). However, most of them observed in the field represent erosional relicts, that can either occur alongside porphyry-Cu deposits, and therefore over the propylitic altered rocks, or partly or fully overlie and hide the porphyry deposit itself (Sillitoe, 2010, and references therein). The zoned mineral pattern resulting from the spectral mineral mapping may, therefore, reflect shallower levels of the typical vertical zonation described in the literature for lithocaps (Sillitoe, 2010), as graphically described in the schematic section in Fig. 12b.

Alternatively, the shown pattern could represent a minor, independent and distal expression of the wider porphyry- or IOCG intrusion-related system, or be part of a now eroded and/or partly covered larger advanced argillic zone (like for example Red Mountain, Northern Patagonia; Berger et al., 2003), which could occur alongside porphyry-Cu centers or above large IOCGs of the Coastal Cordillera (see Sillitoe and Perelló, 2005; Chen, 2013). An important indicator for buried and partly weathered mineralization occurrences is the presence of high 900D values (and locally high 1480D values), thus indicating high Fe^{3+}-bearing mineral phases (i.e., goethite, jarosite) typically found in limonitic leached caps associated with Cu deposits (Taylor, 2011). In the new target area, the abundance band ratio (centered at 913 nm; e.g., Laukamp, 2022; Chirico et al., 2022) allows to map a quite extensive zone likely characterized by the presence of goethite + jarosite likely overlying buried sulfides (Fig. 12).

5.2. Comparison with other spaceborne optical sensors

Previous studies have successfully demonstrated the applications of optical satellite imagery for mineral exploration at regional scale. Nonetheless, more comprehensive remote-based assessments of mineral compositions typically rely on costlier airborne hyperspectral surveys (e.g., Berger et al., 2003, by using AVIRIS airborne data; Kokaly et al., 2017a, by using HyMap data) as opposed to other multispectral satellite applications, even though the valuable design of sensors like ASTER or WV-3, incorporating specific spectral bands sensitive to key alteration types, has facilitated the mapping of potentially valuable mineral information for exploration since early 2000 s. As also demonstrated by Laukamp (2022), PRISMA spaceborne hyperspectral imagery provides mineral mapping capabilities, in some cases, comparable to hyperspectral airborne imagery, although with reduced spatial resolution (PRISMA VNIR-SWIR = 30 m/pixel; common airborne sensors 7 m/pixel up to 1 m/pixel). The reason is the intrinsic hyperspectral character of PRISMA (171 SWIR bands at SNR $\geq$ 100 at wavelengths larger than 2000 nm, Cogliati et al., 2021), compared to the coarser spectral resolution of other commonly used satellite multispectral sensors, such as ASTER and WV-3 (Zhang et al., 2016; Chen et al., 2021). Previous studies have shown that ASTER SWIR bands can separate mineral groups associated with advanced argillic (alunite, kaolinite, dickite, pyrophyllite), phyllic (sericite and illite) and propylitic alterations (carbonate, epidote and chlorite) (Abrams and Yamaguchi, 2019). Several studies have shown that WV-3 allows detailed mineral and lithological mapping (Kruse and Perry, 2013). The results of band rationing applied to WV-3 VNIR–SWIR data showed that it allows mapping and differentiating chlorite + epidote assemblages, as well as kaolinite and montmorillonite because of its finer spatial and spectral resolutions in SWIR region, compared to ASTER data (Salehi and Tangestani, 2020). Indeed, the remote detection of < 10 to 20 nm wavelength changes, such as the precise measurement of white mica Tschermak substitution at the 2200 nm feature and the alunite K-Na composition at the 1480 nm feature, necessitates a spectral resolution of <=20 nm. Multispectral systems with SWIR-2 spectral resolutions exceeding 40 nm, like ASTER and WV-3, are ill-suited for this purpose, making hyperspectral data a more suitable choice (Cudahy, 2016).

The PRISMA imagery demonstrates the potential of hyperspectral satellite data for mineral exploration with regards to accurate mineral mapping, which is a key factor for successful mineral exploration. Regarding its performances, even after the latest upgrades on both the L1 and L2 processors performed by ASI, aimed to solve errors and increase the overall data quality (see PRISMA Latest News on https:

//www.prisma.asi.it), the striping effect affecting several SWIR bands is still present. However, the "fluctuating" pattern observed by previous authors (e.g. Laukamp, 2022; Chirico et al., 2022) in the VNIR wavelength region when mapping the Fe-oxides and hydroxides, perhaps caused by the applied spectral resampling during the smile correction processing within the L1 processor (Cogliati et al., 2021), has been significantly reduced. Looking toward the future, the upcoming PRISMA second generation mission, along with other hyperspectral missions in operational phase and announced for the next few years, hold promise for advancing capabilities in this field.

6. Conclusions

The PRISMA satellite hyperspectral imagery was analyzed for testing its performances in the identification of outcropping hydrothermal and supergene alteration zones related to IOCG and porphyry-Cu(-Mo) ore deposits in the Chilean Andes at two different test sites: the Marimaca Copper Project in the Naguayán district (Antofagasta region) and the Río Blanco-Los Bronces district (Santiago region), with a focus on the Los Sulfatos deposit. PRISMA can be used for this purpose because hydrothermal and supergene alteration minerals exhibit distinct and diagnostic spectral signatures within the wavelength ranges detected by the sensor, serving as a supportive tool for identifying and mapping target mineral phases. In exploration phases, it may aid in defining zonation based on the mineral associations and their respective compositional variability, laying the groundwork for guiding subsequent ground-based investigations. Alteration minerals that are optically active in the VNIR region, such as supergene products like Fe-oxides/hydroxides and sulfates (jarosite), as well as in the SWIR range, such as hydrothermal minerals associated with advanced argillic (Na-rich alunite, K-rich-alunite and kaolinite), phyllic (white micas, such as muscovite and phengite), propylitic and potassic alteration (chlorite, epidote and biotite), were detected in both the test sites. The results show that PRISMA data are valuable for mineral exploration studies, as the data can be acquired over large areas, where new exploration targets may be delineated. The spectral mineral mapping results provided in this study confirm what was previously mapped in the field in the Río Blanco-Los Bronces district with a high accuracy. Moreover, it offered new information in alteration assemblages vectoring to the mineralized bodies in the Naguayán district, potentially identifying previously unknown or underestimated exploration targets that require further geochemical follow-up surveys. The narrower SWIR bands of PRISMA have demonstrated their effectiveness in distinguishing compositional features between spectrally similar minerals, such as white micas, kaolinite-group minerals, and sulfates (e.g., alunite), when compared to spaceborne multispectral sensors with coarser spectral resolution. In fact, the spectral capabilities achieved with PRISMA are comparable to those of finer spatial resolution hyperspectral surveys (such as airborne), which typically involve much higher costs and resource requirements. Moreover, the detection of the alunite-kaolinite spectral class that is confined to a relatively small area in the Marimaca area, is an indicator that the 30 m spatial resolution spaceborne PRISMA data can be successfully used also for the detection of minor remote exploration targets.

Declaration of competing interest

The authors declare that they have no financial interests/personal relationships which may be considered as potential competing interests that could have influenced the work reported in this paper.

Data availability

Project carried out using PRISMA Products, © of the Italian Space Agency (ASI), delivered under an ASI License to use. The redistribution of products to any third party is not allowed.

Acknowledgments

This paper was produced in the frame of the Ph.D. projects of Dr R. Chirico (Ph.D. scholarships Complementary Operational Program - POC "Research and Innovation 2014–2020") and A. Sorrentino (Ph.D. scholarships of the Programma Operativo Nazionale - PON "Research and Innovation 2014–2020"), co-financed by the Italian Ministry of University and Research and European Social Fund (ESF) 2014–2020; Supervisor: Professor Nicola Mondillo. Part of the work was performed for the M.Sc. thesis of F. Corrado. The work was partly funded in the framework of I_ProMoNaLISA project by the University Research Funding Program-Line A of the University of Naples Federico II, Scientific Responsible: Professor Diego Di Martire. The authors are grateful to the Ore Geology Reviews Editor-in-Chief Professor Huayong Chen, and to the Associate Editor Dr D. Müller and the anonymous reviewer, for the constructive comments and suggestions that have significantly improved the quality of the manuscript.

Data access and data availability.

Project carried out using PRISMA Products, © of the Italian Space Agency (ASI), delivered under an ASI License to use by visiting prisma.asi.it.

On request, high-resolution images of the PRISMA mineral maps for the investigated areas can be provided.

Appendix A. Supplementary data

Supplementary data to this article can be found online at https://doi.org/10.1016/j.oregeorev.2024.105998.

References

Abrams, M.J., Yamaguchi, Y., 2019. Twenty years of ASTER contributions to lithologic mapping and mineral exploration. Remote Sens. (Basel) 11, 1394.
Abrams, M.J., Brown, D., Lepley, L., Sadowski, R., 1983. Remote sensing for porphyry copper deposits in southern Arizona. Econ. Geol. 78, 591–604.
Agenzia Spaziale Italiana (ASI) (2020) PRISMA Products Specification Document Issue 2.1 Date 12/03/2020.
Arbiol, C., Layne, G.D., 2021. Raman spectroscopy coupled with reflectance spectroscopy as a tool for the characterization of key hydrothermal alteration minerals in epithermal Au–Ag systems: utility and implications for mineral exploration. Appl. Spectrosc. 75, 1475–1496.
Barra, F., Reich, M., Selby, D., et al., 2017. Unraveling the origin of the andean IOCG clan: a re-os isotope approach. Ore Geol. Rev. 81, 62–78.
Beckinsale R, Sanchez-Fernandez A, Brook M, et al., 1985. Rb-Sr whole-rock isochron and K-Ar age determinations for the Coastal Batholith of Peru. pp. 177–202.
Bedini, E., 2017. The use of hyperspectral remote sensing for mineral exploration: a review. J. Hyperspectral Remote Sens. 7, 189–211.
Bedini, E., Chen, J., 2020. Application of PRISMA satellite hyperspectral imagery to mineral alteration mapping at cuprite, Nevada, USA. J. Hyperspectral Remote Sens. 10, 87–94.
Benavides, J., Kyser, T., Clark, A.H., et al., 2007. The mantoverde iron oxide-copper-gold district, III región, Chile: the role of regionally derived, nonmagmatic fluids in chalcopyrite mineralization. Econ. Geol. 102, 415–440.
Berger, B.R., King, T.V., Morath, L.C., Phillips, J.D., 2003. Utility of high-altitude infrared spectral data in mineral exploration: application to northern Patagonia Mountains, Arizona. Econ. Geol. 98, 1003–1018.
Bishop, J., Lane, M., Dyar, M., Brown, A., 2008. Reflectance and emission spectroscopy study of four groups of phyllosilicates: smectites, kaolinite-serpentines, chlorites and micas. Clay Miner. 43, 35–54.
Bishop, J.L., Murad, E., 2005. The visible and infrared spectral properties of jarosite and alunite. Am. Mineral. 90, 1100–1107.
Bouzari, F., Clark, A.H., 2002. Anatomy, evolution, and metallogenic significance of the supergene orebody of the cerro Colorado porphyry copper deposit, I región, northern Chile. Econ. Geol. 97, 1701–1740.
Burns, R.G., 1993. Mineralogical applications of crystal field theory. In: Topics in Mineral Physics and Chemistry, , Second edition5. Cambridge University Press, Cambridge. https://doi.org/10.1017/CBO9780511524899.
Cabello, J., 2021. Gold deposits in Chile. andean. Geology 48, 1–23.
Chang, Z., Hedenquist, J.W., White, N.C., et al., 2011. Exploration tools for linked porphyry and epithermal deposits: example from the mankayan intrusion-centered cu-au district, Luzon, Philippines. Econ. Geol. 106, 1365–1398.
Chen, H., 2013. External sulphur in IOCG mineralization: implications on definition and classification of the IOCG clan. Ore Geol. Rev. 51, 74–78.
Chen, Q., Zhao, Z., Zhou, J., et al., 2021. New insights into the pulang porphyry copper deposit in southwest China: indication of alteration minerals detected using ASTER and WorldView-3 data. Remote Sens. (Basel) 13, 2798.

Chirico, R., Mondillo, N., Laukamp, C., et al., 2022. Mapping hydrothermal and supergene alteration zones associated with carbonate-hosted Zn-Pb deposits by using PRISMA satellite imagery supported by field-based hyperspectral data, mineralogical and geochemical analysis. Ore Geol. Rev. 152, 105244.
Clark, A.H., Farrar, E., Kontak, D.J., et al., 1990a. Geologic and geochronologic constraints on the metallogenic evolution of the Andes of southeastern Peru. Econ. Geol. 85, 1520–1583.
Clark, R.N., King, T.V., Klejwa, M., et al., 1990b. High spectral resolution reflectance spectroscopy of minerals. J. Geophys. Res. Solid Earth 95, 12653–12680.
Cogliati, S., Sarti, F., Chiarantini, L., et al., 2021. The PRISMA imaging spectroscopy mission: overview and first performance analysis. Remote Sens. Environ. 262, 112499.
Corriveau, L., 2007. Iron oxide copper-gold (±Ag±Nb±P±REE±U) deposits: a Canadian perspective. Mineral Deposits of Canada: A Synthesis of Major Deposit-Types, District Metallogeny, the Evolution of Geological Provinces, and Exploration Methods: Geological Association of Canada, Mineral Deposits Division, Special Publication 5, 265–278.
Cortés, J., Marquardt, C., González, G., Wilke, H., Marinovic, N., 2007. Cartas Mejillones y Península de Mejillones, Región de Antofagasta., Carta Geológica de Chile, Serie Geología Básica, 103 y 104, 58 p., 1 mapa escala 1: 100.000.
Cotton III, W.B., 2003. Near infrared and XRD quantification of porphyry copper alteration at cerro Colorado and Spence. Faculty of the Graduate School of the University of Colorado, Chile, p. 236.
Crowley, J., Williams, D., Hammarstrom, J., et al., 2003. Spectral reflectance properties (0.4–2.5 μm) of secondary fe-oxide, fe-hydroxide, and fe-sulphate-hydrate minerals associated with sulphide-bearing mine wastes. geochemistry: exploration. Environ. Anal. 3, 219–228.
Cudahy, T., 2016. Mineral mapping for exploration: an Australian journey of evolving spectral sensing technologies and industry collaboration. Geosciences 6, 52.
Cudahy, T., Jones, M., Thomas, M., Laukamp, C., Caccetta, M., Hewson, R., Rodger, A., Verrall, M., 2008. Next generation mineral mapping. Queensland Airborne HyMap and Satellite ASTER Surveys 2006–2008. Commonwealth Scientific and Industrial Research Organization Report P2007/364.
Cudahy, T., Ramanaidou, E., 1997. Measurement of the hematite: goethite ratio using field visible and near-infrared reflectance spectrometry in channel iron deposits, Western Australia. Aust. J. Earth Sci. 44, 411–420.
Curtiss, B., 1985. Evaluation of the physical properties of naturally occurring iron (III) oxyhydroxides on rock surfaces in arid and semi-arid regions using visible and near infrared reflectance spectroscopy (PhD Thesis).
Deckart, K., Clark, A.H., Celso, A.A., et al., 2005. Magmatic and hydrothermal chronology of the giant Río Blanco porphyry copper deposit, central Chile: implications of an integrated U-pb and 40Ar/39Ar database. Econ. Geol. 100, 905–934.
Deckart, K., Silva, W., Spröhnle, C., Vela, I., 2014. Timing and duration of hydrothermal activity at the los bronces porphyry cluster: an update. Miner. Deposita 49, 535–546.
Duke, E.F., 1994. Near infrared spectra of muscovite, tschermak substitution, and metamorphic reaction progress: implications for remote sensing. Geology 22, 621–624.
Frost, R.L., Johansson, U., 1998. Combination bands in the infrared spectroscopy of kaolins—a drift spectroscopic study. Clay Clay Miner. 46, 466–477.
García, M., Maksaev, V., Townley, B., Dilles, J., 2017. Metallogeny, structural evolution, post-mineral cover distribution and exploration in concealed areas of the northern chilean Andes. Ore Geol. Rev. 86, 652–672.
Gendall, I.R., Quevedo, L.A., Sillitoe, R.H., et al., 2000. Discovery of a jurassic porphyry copper belt, pangui area, southern Ecuador. SEG Discovery 1–15.
Graham, G.E., Kokaly, R.F., Kelley, K.D., et al., 2018. Application of imaging spectroscopy for mineral exploration in Alaska: a study over porphyry cu deposits in the eastern Alaska range. Econ. Geol. 113, 489–510.
Groves, D.I., Bierlein, F.P., Meinert, L.D., Hitzman, M.W., 2010. Iron oxide copper-gold (IOCG) deposits through Earth history: implications for origin, lithospheric setting, and distinction from other epigenetic iron oxide deposits. Econ. Geol. 105, 641–654.
Guanter, L., Irakulis-Loitxate, I., Gorroño, J., et al., 2021. Mapping methane point emissions with the PRISMA spaceborne imaging spectrometer. Remote Sens. Environ. 265, 112671.
Halley, S., Dilles, J.H., Tosdal, R.M., 2015. Footprints: Hydrothermal alteration and geochemical dispersion around porphyry copper deposits. SEG newsletter 1–17.
Harraden, C.L., Mcnulty, B.A., Gregory, M.J., Lang, J.R., 2013. Shortwave infrared spectral analysis of hydrothermal alteration associated with the pebble porphyry copper-gold-molybdenum deposit, Iliamna, Alaska. Econ. Geol. 108, 483–494.
Hedenquist, J.W., Arribas, A., 2022. Exploration implications of multiple formation environments of advanced argillic minerals. Econ. Geol. 117, 609–643. https://doi.org/10.5382/econgeo.4880.
Heller Pearlshtien, D., Pignatti, S., Greisman-Ran, U., Ben-Dor, E., 2021. PRISMA sensor evaluation: a case study of mineral mapping performance over makhtesh Ramon, Israel. Int. J. Remote Sens. 42, 5882–5914.
Hitzman, M.W., Oreskes, N., Einaudi, M.T., 1992. Geological characteristics and tectonic setting of proterozoic iron oxide (cu - U - au - REE) deposits. Precambr. Res. 58, 241–287.
Irarrazaval, V., Sillitoe, R.H., Wilson, A.J., et al., 2010. Discovery history of a giant, high-grade, hypogene porphyry copper-molybdenum deposit at Los Sulfatos, Los Bronces-Río Blanco district, central Chile. Society of Economic Geologists, p. 0.
Ishagh, M.M., Pour, A.B., Benali, H., et al., 2021. Lithological and alteration mapping using landsat 8 and ASTER satellite data in the reguibat shield (west african craton), north of Mauritania: implications for uranium exploration. Arab. J. Geosci. 14, 2576.
Kalanchey, R., Castillo, A.F., Weston, A.S., et al., 2020. NI 43 101 technical report. Preliminary economic assessment Marimaca Project Antofagasta, II Region, Chile.
Kerr, A., Rafuse, H., Sparkes, G., Hinchey, J., Sandeman, H., 2011. Visible/infrared spectroscopy (VIRS) as a research tool in economic geology; background and pilot studies from new foundland and Labrador. Geological Survey, Report 11.
Kokaly, R., Clark, R., Swayze, G., Livo, K., Hoefen, T., Pearson, N., Wise, R., Benzel, W., Lowers, H., Driscoll, R., 2017b. Usgs spectral library version 7 data: us geological survey data release. United States Geological Survey (USGS).
Kokaly, R.F., Graham, G.E., Hoefen, T.M., Kelley, K.D., Johnson, M.R., Hubbard, B.E., Buchhorn, M., Prakash, A., 2017a. Multiscale hyperspectral imaging of the Orange Hill porphyry copper deposit, Alaska, USA, with laboratory-, field-, and aircraft-based imaging spectrometers. Presented at the Proc. Explor, Toronto, Spectral Geology and Remote Sensing, pp. 923–943.
Kopackova-Strnadova, V., Giebel, R.J., Rapprich, V., Magna, T., 2023. Testing prisma capability to detect Rare Earth element contents from space. In: In: IGARSS 2023–2023 IEEE International Geoscience and Remote Sensing Symposium. IEEE, pp. 7610–7613.
Kramer, W., Siebel, W., Romer, R.L., et al., 2005. Geochemical and isotopic characteristics and evolution of the jurassic volcanic arc between Arica (18 30′ S) and Tocopilla (22 S), north chilean coastal cordillera. Geochemistry 65, 47–78.
Kreiner, D.C., Barton, M.D., 2017. Sulfur-poor intense acid hydrothermal alteration: a distinctive hydrothermal environment. Ore Geol. Rev. 88, 174–187.
Kruse, F.A., Perry, S.L., 2013. Mineral mapping using simulated Worldview-3 short-wave-infrared imagery. Remote Sens. (Basel) 5, 2688–2703.
Ladino, M., Tomlinson, A., Blanco, N., 1997. Nuevos antecedentes para la edad de la deformación cretácica en sierra de Moreno, II región de Antofagasta, norte de Chile. Presented at the VIII Congreso Geológico Chileno, Antofagasta 1, 103–107.
Lang, J.R., Thompson, J., 2001. Alkalic porphyry cu-au deposits: magmatic-hydrothermal mineralization with similarities to feoxide cu-au deposits. Presented at the Geological Society of America, Abstracts with Programs, p. 15.
Larson, R.L., 1991. Geological consequences of superplumes. Geology 19, 963–966. https://doi.org/10.1130/0091-7613(1991)019<0963:GCOS>2.3.CO;2.
Laukamp, C., 2022. Geological mapping using mineral absorption feature-guided band-ratios applied to prisma satellite hyperspectral level 2D imagery. IEEE 5981–5984.
Laukamp, C., Cudahy, T., Thomas, M., et al., 2011. Hydrothermal mineral alteration patterns in the Mount Isa inlier revealed by airborne hyperspectral data. Aust. J. Earth Sci. 58, 917–936.
Laukamp, C., Rodger, A., LeGras, M., et al., 2021. Mineral physicochemistry underlying feature-based extraction of mineral abundance and composition from shortwave, mid and thermal infrared reflectance spectra. Minerals 11, 347.
Llaumett, C., Olcay, L., Marin, C., Marquardt, J.C., Reyes, E., 1975. El yacimiento cobre porfídico Andacollo, provincia de Coquimbo, Chile. Revista Geológica De Chile 2, 56–66.
Maksaev, V., Munizaga, F., McWilliams, M., et al., 2004. New chronology for el teniente, chilean Andes, from U-pb, 40Ar/39Ar, re-os, and fission-track dating: implications for the evolution of a supergiant porphyry cu-mo deposit. Society of Economic Geologists 11, 15–54.
Marimaca Copper Corp. 2023. Regulatory News. Available online: https://marimaca.com/regulatory-news/ (accessed on 23 January 2022).
Mars, J.C., Rowan, L.C., 2006. Regional mapping of phyllic-and argillic-altered rocks in the zagros magmatic arc, Iran, using advanced spaceborne thermal emission and reflection radiometer (ASTER) data and logical operator algorithms. Geosphere 2, 161–186.
Marschik, R., Fontboté, L., 2001. The Candelaria-punta del cobre iron oxide cu-au (-zn-ag) deposits, Chile. Econ. Geol. 96, 1799–1826.
Maureira, I., Barra, F., Reich, M., Palma, G., 2022. Geology of the Altamira and las luces deposits, coastal cordillera, northern Chile: implications for the origin of stratabound Cu–(Ag) deposits. Miner. Deposita 1–24.
McLeod, R., Gabell, A., Green, A., Gardavsky, V., 1987. Chlorite infrared spectral data as proximity indicators of volcanogenic massive sulphide mineralisation. International congress on the geology, structure, mineralisation and economics of Pacific Rimp. p. 321–324.
Meyer, J.M., Kokaly, R.F., Holley, E., 2022. Hyperspectral remote sensing of white mica: a review of imaging and point-based spectrometer studies for mineral resources, with spectrometer design considerations. Remote Sens. Environ. 275, 113000.
Morris, R.V., Lauer Jr, H.V., Lawson, C.A., et al., 1985. Spectral and other physicochemical properties of submicron powders of hematite (α-Fe2O3), maghemite (γ-Fe2O3), magnetite (Fe3O4), goethite (α-FeOOH), and lepidocrocite (γ-FeOOH). J. Geophys. Res. Solid Earth 90, 3126–3144.
Mpodozis, C., Ramos, V., 1989. The Andes of Chile and Argentina. In: Geology of the Andes and its Relation to Hydrocarbon and Mineral Resources, vol. 11. Earth Sciences Series, pp. 59–90.
Munizaga, F., Huete, C., Hervé, F., 1985. Geocronología K-ar y razones iniciales 87Sr/86Sr de la franja pacífica de Desarrollos hidrotermales. In: Presented at the Proceedings IV Congreso Geológico Chileno, pp. 357–379.
Noble, D.C., McKee, E.H., 1999. The miocene metallogenic belt of central and northern Peru. Society of Economic Geologists Special Publication 7, 155–193.
Ossandón, C.G., Fréraut, C.R., Gustafson, L.B., et al., 2001. Geology of the Chuquicamata mine: a progress report. Econ. Geol. 96, 249–270.
Oviedo, L., 2017. Technical report for the Marimaca Copper Project, Antofagasta Province, Region II, Chile: technical report prepared by NCL Ingeniería y Construcción SpA for Marimaca Copper Mining, effective date 24 February 2017, p. 99.
Oviedo, L., 2022. Updated Mineral Resource Estimation for the Marimaca Copper Project, Antofagasta Province, Region II, Chile: technical report prepared by NCL Ingeniería y Construcción SpA for Marimaca Copper Mining, effective date 26 November 2022, p. 217.

Padilla-Garza, R.A., Titley, S.R., Eastoe, C.J., 2005. Hypogene evolution of the escondida porphyry copper deposit, Chile. Society of Economic Geologists Special Publication 11, 141–165.
Peyghambari, S., Zhang, Y., 2021. Hyperspectral remote sensing in lithological mapping, mineral exploration, and environmental geology: an updated review. J. Appl. Remote Sens. 15, 031501.
Piquer, J., Skarmeta, J., Cooke, D.R., 2015. Structural evolution of the rio Blanco-los Bronces District, Andes of Central Chile: controls on stratigraphy, magmatism, and mineralization. Econ. Geol. 110, 1995–2023.
Pollard, P., 2000. In: Porter, T.M. (Ed.), Hydrothermal Iron Oxide Copper-Gold and Related Deposits: A Global Perspective, 1. PGC Publishing, pp. 27–41.
Portela, B., Sepp, M.D., van Ruitenbeek, F.J., Hecker, C., Dilles, J.H., 2021. Using hyperspectral imagery for identification of pyrophyllite-muscovite intergrowths and alunite in the shallow epithermal environment of the Yerington porphyry copper district. Ore Geol. Rev. 131, 104012.
Pour, A.B., Hashim, M., 2012. The application of ASTER remote sensing data to porphyry copper and epithermal gold deposits. Ore Geol. Rev. 44, 1–9.
PRISMA data portal, n.d. Available online: https://prisma.asi.it/.
Ramírez, L.E., Palacios, C., Townley, B., et al., 2006. The mantos blancos copper deposit: an upper jurassic breccia-style hydrothermal system in the coastal range of northern Chile. Miner. Deposita 41, 246–258.
Ricardo, V.R., Gustafson, L.B., Vukasovic, M., et al., 1999. Ore breccias in the rio Blanco-los bronces porphyry copper deposit, Chile. Society of Economic Geologists, Geology and Ore Deposits of the Central Andes.
Richards, J.P., 2009. Postsubduction porphyry cu-au and epithermal au deposits: products of remelting of subduction-modified lithosphere. Geology 37, 247–250.
Richards, J.P., Mumin, A.H., 2013. Magmatic-hydrothermal processes within an evolving Earth: iron oxide-copper-gold and porphyry cu-mo-au deposits. Geology 41, 767–770.
Riley, D., Cudahy, T., Hewson, R., Jansing, D., Hackwell, J., 2007. SEBASS imaging for copper porphyry and skarn deposits, Yerington, NV. In: Presented at the Proceedings of Exploration 07: Fifth Decennial International Conference on Mineral Exploration, pp. 1151–1157.
Romaniello, V., Spinetti, C., Silvestri, M., Buongiorno, M.F., 2021. A methodology for CO2 retrieval applied to hyperspectral PRISMA data. Remote Sens. (Basel) 13, 4502.
Romaniello, V., Buongiorno, M.F., Spinetti, C., Silvestri, M., 2022. Analysis of volcanic Carbon dioxide emissions by means of prisma hyperspectral data and in situ measurements. IEEE 7268–7271.
Rowland, M., Clark, A.H., 2001. Temporal overlap of supergene alteration and high-sulfidation mineralization in the Spence porphyry copper deposit, II región, Chile [abs.]. In: Presented at the Geological Society of America, Abstracts with Programs, p. p. A-358..
Salehi, T., Tangestani, M.H., 2020. Per-pixel analysis of ASTER data for porphyry copper hydrothermal alteration mapping: a case study of NE Isfahan. Iran. Remote Sensing Applications: Society and Environment 20, 100377.
Scheuber, E., Andriessen, P.A., 1990. The kinematic and geodynamic significance of the Atacama fault zone, northern Chile. J. Struct. Geol. 12, 243–257.
Serrano, L., Vargas, R., Stambuk, V., Aguilar, C., Galeb, M., Holmgren, C., Contreras, A., Godoy, S., Vela, I., Skewes, M.A., Stern, C.R., 1998. In: Camus, F., Sillitoe, R.M., Petersen, R. (Eds.), Andean Copper Deposits: New Discoveries, Mineralization, Styles and Metallogeny, 5. Society of Economic Geologists. Special Pubblication, pp. 119–130. https://doi.org/10.5382/SP.05.09.
Sillitoe, R.H., 1972. A plate tectonic model for the origin of porphyry copper deposits. Econ. Geol. 67, 184–197.
Sillitoe, R., 1988. Epochs of intrusion-related copper mineralization in the Andes. J. S. Am. Earth Sci. 1, 89–108.
Sillitoe, R.H., 2003. Iron oxide-copper-gold deposits: an andean view. Miner. Deposita 38, 787–812.
Sillitoe, R.H., 2005. Supergene oxidized and enriched porphyry copper and related deposits. In: Economic Geology 100th Anniversary Volume 723–768. https://doi.org/10.5382/AV100.22.
Sillitoe, R.H., 2010. Porphyry Copper Systems. Economic Geology 105, 3–41. https://doi.org/10.2113/gsecongeo.105.1.3.
Sillitoe, R.H., Perelló, J., 2005. Andean Copper Province: Tectonomagmatic Settings, Deposit Types, Metallogeny, Exploration, and Discovery. In: One Hundredth Anniversary Volume. Society of Economic Geologists, p. 0. https://doi.org/10.5382/AV100.26.
Sillitoe, R.H., Jaramillo, L., Damon, P.E., et al., 1982. Setting, characteristics, and age of the andean porphyry copper belt in Colombia. Econ. Geol. 77, 1837–1850.
Skewes, M.A., Arévalo, A., Floody, R., Zuñiga, P.H., Stern, C.R., 2002. The Giant El Teniente Breccia Deposit: Hypogene Copper Distribution and Emplacement. In: Goldfarb, R.J., Nielsen, R.L. (Eds.), Integrated Methods for Discovery: Global Exploration in the Twenty-First Century. Society of Economic Geologists. https://doi.org/10.5382/SP.09.14.
Spatz, D.M., 1996. Remote sensing strategies for mineral exploration and development: the precious metal and porphyry deposit models. International Archives of Photogrammetry and Remote Sensing 31, 638–649.
Stoffregen, R.E., Cygan, G.L., 1990. An experimental study of na-K exchange between alunite and aqueous sulfate solutions. Am. Mineral. 75, 209–220.
Tangestani, M., Moore, F., 2002. Porphyry copper alteration mapping at the meiduk area. Iran. International Journal of Remote Sensing 23, 4815–4825.
Tappert, M.C., Rivard, B., Giles, D., et al., 2013. The mineral chemistry, near-infrared, and mid-infrared reflectance spectroscopy of phengite from the olympic dam IOCG deposit, South Australia. Ore Geol. Rev. 53, 26–38.
Taranik, J.V., Aslett, Z.L., 2009. Development of Hyperspectral Imaging for Mineral Exploration. In: Bedell, R., Crósta, A.P., Grunsky, E. (Eds.), Remote Sensing and Spectral Geology. Society of Economic Geologists, p. 0. https://doi.org/10.5382/Rev.16.07.
Taylor, R., 2011. Gossans and leached cappings: field assessment. Springer Science & Business Media, p. 165.
Thiele, S.T., Lorenz, S., Kirsch, M., et al., 2021. Multi-scale, multi-sensor data integration for automated 3-D geological mapping. Ore Geol. Rev. 136, 104252.
Thompson, A.J., Hauff, P., Robitaille, A., 1999. Alteration mapping in exploration: application of short-wave Infrared (SWIR) spectroscopy. Society of Economic Geologists Newsletter 39, 16–27. https://doi.org/10.5382/SEGnews.1999-39.fea.
Toro, J.C., Ortúzar, J., Zamorano, J., et al., 2012. Protracted magmatic-hydrothermal history of the Río Blanco-Los Bronces district, Central Chile: Development of world's greatest known concentration of copper. Society of Economic Geologists, p. 0.
van Ruitenbeek, F.J., Cudahy, T., Hale, M., van der Meer, F.D., 2005. Tracing fluid pathways in fossil hydrothermal systems with near-infrared spectroscopy. Geology 33, 597–600. https://doi.org/10.1130/G21375.1.
Vedder, W., McDonald, R.S., 1963. Vibrations of the OH ions in muscovite. J. Chem. Phys. 38, 1583–1590.
Velde, B., 1965. Phengite micas; synthesis, stability, and natural occurrence. Am. J. Sci. 263, 886–913.
Wang, R., Cudahy, T., Laukamp, C., et al., 2017. White mica as a hyperspectral tool in exploration for the sunrise dam and kanowna belle gold deposits, Western Australia. Econ. Geol. 112, 1153–1176.
Warnaars, F.W., Holmgren, D.C., Barassi, F.S., 1985. Porphyry copper and tourmaline breccias at los bronces-rio Blanco, Chile. Econ. Geol. 80, 1544–1565.
White, A.J., Laukamp, C., Stokes, M.A., et al., 2017. Vibrational spectroscopy of epidote, pumpellyite and prehnite applied to low-grade regional metabasites. geochemistry: exploration. Environment, Analysis 17, 315–333.
Williams P.J., Barton M.D., Johnson D.A., et al., 2005. Iron oxide copper-gold deposits: Geology, space-time distribution, and possible modes of origin.
Wilson, N., Zentilli, M., Reynolds, P., Boric, R., 2003. Age of mineralization by basinal fluids at the el soldado manto-type copper deposit, Chile: 40Ar/39Ar geochronology of K-feldspar. Chem. Geol. 197, 161–176.
Zadeh, M.H., Tangestani, M.H., Roldan, F.V., Yusta, I., 2014. Sub-pixel mineral mapping of a porphyry copper belt using EO-1 Hyperion data. Adv. Space Res. 53, 440–451.
Zentilli, M., 2022. Historia, Exploración y geología de los yacimientos metalíferos de Chile 900–2021. (Francisco camus I. and Juan Carlos Castelli S.). Econ. Geol. 117, 1675–1676.
Zhang, M., Wang, L., Hirai, S., et al., 2005. Dehydroxylation and CO2 incorporation in annealed mica (sericite): an infrared spectroscopic study. Am. Mineral. 90, 173–180.
Zhang, T., Yi, G., Li, H., et al., 2016. Integrating data of ASTER and Landsat-8 OLI (AO) for hydrothermal alteration mineral mapping in duolong porphyry cu-au deposit, tibetan plateau. China. Remote Sensing 8, 890.